Kinetic-scale current sheets in the solar wind at 5 AU

I.Y. Vasko[1,2], K. Alimov[3], T.D. Phan[3], F.S. Mozer[3], and A.V. Artemyev[2,4]

[1]William B. Hanson Center for Space Sciences, University of Texas at Dallas, Richardson, TX, USA
[2]Space Research Institute of Russian Academy of Sciences, Moscow, Russia
[3]Space Science Laboratory, University of California, Berkeley, California, USA
[4]Department of Earth, Planetary, and Space Sciences, University of California, Los Angeles, California, USA

Key Points:

- Current sheets are predominantly rotations of the magnetic field on proton kinetic scales
- Scale-invariant properties strongly indicate that current sheets are produced by turbulence
- The asymmetry of current sheets is typically insufficient to suppress magnetic reconnection

Corresponding author: Ivan Y. Vasko, `Ivan.Vasko@UTDallas.edu`

Abstract

We present statistical analysis of 16,903 current sheets (CS) observed over 641 days aboard Ulysses spacecraft at 5 AU. We show that the magnetic field rotates across CSs through some shear angle, while only weakly varies in magnitude. The CSs are typically asymmetric with statistically different, though only by a few percent, magnetic field magnitudes at the CS boundaries. The dataset is classified into about 90.6% non-bifurcated and 9.4% bifurcated CSs. Most of the CSs are proton kinetic-scale structures with the half-thickness of non-bifurcated and bifurcated CSs within respectively 200–2,000 km and 500–5,000 km or 0.5–5λ_p and 0.7–15λ_p in units of local proton inertial length. The amplitude of the current density, mostly parallel to magnetic field, is typically within 0.05–0.5 nA/m^2 or 0.04–0.4J_A in units of local Alfvén current density. The CSs demonstrate approximate scale-invariance with the shear angle and current density amplitude scaling with the half-thickness, $\Delta\theta \approx 16.6^\circ\ (\lambda/\lambda_p)^{0.34}$ and $J_0/J_A \approx 0.14\ (\lambda/\lambda_p)^{-0.66}$. The matching of the magnetic field rotation and compressibility observed within the CSs against those in ambient solar wind indicate that the CSs are produced by turbulence, inheriting thereby its scale-invariance and compressibility. The estimated asymmetry in plasma beta between the CS boundaries is shown to be insufficient to suppress magnetic reconnection through the diamagnetic drift of X-line, but magnetic reconnection is probably suppressed by other processes. The presented results will be of value for future comparative analysis of CSs observed at different distances from the Sun.

Plain Language Summary

Current sheets are coherent structures potentially contributing into solar wind heating. These structures are highly-likely produced by turbulence, but the alternative hypothesis of coronal origin has not been ruled out. The analysis of current sheets at different distances from the Sun may potentially shed light onto the origin and contribution of these structures into solar wind heating. While there are comprehensive analyses of solar wind current sheets at 1 AU and near the Sun, there is still no equivalent analysis of these structures well beyond 1 AU. In this study we present an extensive statistical study of current sheets observed aboard Ulysses around 5 AU. We demonstrate that the current sheets are predominantly rotations of the magnetic field, typically occurring on proton kinetic scales and exhibiting approximate scale-invariance. We provide strong evidence that the current sheets are produced by turbulence and inherit the scale-invariance and magnetic field compressibility typical of turbulence. The presented results will be of value for future comparative analysis of solar wind current sheets observed at different distances from the Sun.

1 Introduction

Solar wind current sheets were observed aboard early spacecraft missions at 0.3–1 AU (Burlaga, 1969; Mariani et al., 1973; Burlaga et al., 1977; Lepping & Behannon, 1986; Söding et al., 2001), 1–8 AU (Tsurutani & Smith, 1979; Tsurutani et al., 1996) and 20 AU (Söding et al., 2001). It was demonstrated that the current sheets are predominantly magnetic field rotations that is the magnetic field rotates across a current sheet through some shear angle, while remains almost constant in magnitude. The early studies used current sheet selection procedures based on magnetic field measurements with the temporal resolution exceeding ten seconds. The current sheets revealed at 1 AU had spatial thickness, computed by assuming the structures are frozen into local plasma flow, larger than about one thousand kilometers or ten proton inertial lengths (Burlaga et al., 1977; Lepping & Behannon, 1986). The typical occurrence rate of current sheets at 1 AU was about one per hour (Mariani et al., 1973; Burlaga et al., 1977) and decreased with increasing radial distance from the Sun (Lepping & Behannon, 1986; Tsurutani & Smith, 1979; Tsurutani et al., 1996). The early studies were heavily focused on classifying current sheets in terms of tangential and rotational discontinuities based on the magnetic field component along the normal computed by Minimum Variance Analysis (MVA). Multi-spacecraft observations showed however that MVA is typically not reliable in estimating the normal to solar wind current sheets and showed that the normal magnetic field component is often within the methodology uncertainty and much smaller than local magnetic field magnitude (Horbury et al., 2001; Knetter et al., 2004; Wang et al., 2024). The latter implies the normal is often almost perpendicular to local background magnetic field in accordance with early theoretical reasoning (Matthaeus et al., 1990; Bieber et al., 1996; Leamon et al., 1998, 2000). The relative occurrence of tangential and rotational discontinuities is still not known (Neugebauer, 2006; Artemyev, Angelopoulos, Vasko, Runov, et al., 2019; Artemyev, Angelopoulos, & Vasko, 2019; Wang et al., 2024). The spacecraft observations and numerical simulations have shown that most of current sheets in the solar wind are produced by turbulence and substantially contribute into development of turbulence cascade as well as solar wind heating (see, e.g., reviews by Matthaeus et al. (2015) and Greco et al. (2018)). Note that a fraction of current sheets, especially large-scale structures, may originate in solar corona (e.g., Borovsky (2008)). The need for understanding plasma turbulence and solar wind heating have recently stimulated comprehensive analyses of solar wind current sheets using high-resolution magnetic field measurements.

Substantial progress has been achieved by the analysis of current sheets at 1 AU using magnetic field measurements with the temporal resolution of 1/3–1/22 s (Vasquez et al., 2007; Perri et al., 2012; Borovsky & Podesta, 2015; Podesta, 2017; Perrone et al., 2017; Borovsky & Burkholder, 2020; Vasko et al., 2021, 2022; Wang et al., 2024). It has been shown that solar wind current sheets are much more abundant than reported in the early studies, their average occurrence rate is about ten per hour, while the half-thickness is typically about 100 km or one proton inertial length (Vasquez et al., 2007; Vasko et al., 2021, 2022; Wang et al., 2024). The early studies missed a substantial fraction of current sheets present at 1 AU, because the selection procedures were based on magnetic field measurements of low temporal resolution and biased to current sheets with larger thickness. The recent analyses have also revealed scale-dependent properties of solar wind current sheets (Vasko et al., 2022; Wang et al., 2024), which along with other arguments (Greco et al., 2008, 2009; Zhdankin et al., 2012) indicate that most of these structures are produced by turbulence. Solar wind current sheets can provide substantial contribution into magnetic field turbulence spectra and affect the break scale between inertial and sub-ion turbulence ranges (Borovsky & Podesta, 2015; Borovsky & Burkholder, 2020). Parker Solar Probe measurements have recently allowed analysis of current sheets around 0.2 AU (Phan et al., 2020; Lotekar et al., 2022). The critical finding of the statistical analysis by Lotekar et al. (2022) is that the properties of current sheets at 0.2 and 1 AU while different in physical units, become essentially identical once normalized to local plasma parameters. Similar extensive analysis of current sheets well beyond 1 AU would be highly valuable for clarifying to what extent current sheet properties at different radial distances are controlled by local plasma parameters.

Several previous studies yielded valuable information about current sheets beyond 1 AU (Tsurutani & Smith, 1979; Tsurutani et al., 1996; Söding et al., 2001; Erdős & Balogh, 2008; Miao et al., 2011; Artemyev et al., 2018). In particular, the previous analyses of current sheets observed aboard Ulysses spacecraft at 5 AU revealed the average occurrence rate of 15–25 current sheets per day (Tsurutani et al., 1996; Erdős & Balogh, 2008; Miao et al., 2011), temporal width from a few to a few tens of seconds (Miao et al., 2011; Tsurutani et al., 1996), spatial half-thickness from about 1,000 to 10,000 km (Erdős & Balogh, 2008), and a positive correlation between the shear angle and temporal width (Miao et al., 2011). A comprehensive study of current sheets at large radial distances is however still necessary for future comparative analyses of current sheets observed at different radial distances. In this paper we present the analysis of current sheets observed aboard Ulysses around 5 AU based on the methodology previously used at 0.2 and 1 AU (Lotekar et al., 2022; Vasko et al., 2021, 2022). Similarly to the latter studies we consider Ulysses observations around solar minimum and almost within the ecliptic plane. The revealed distributions of current

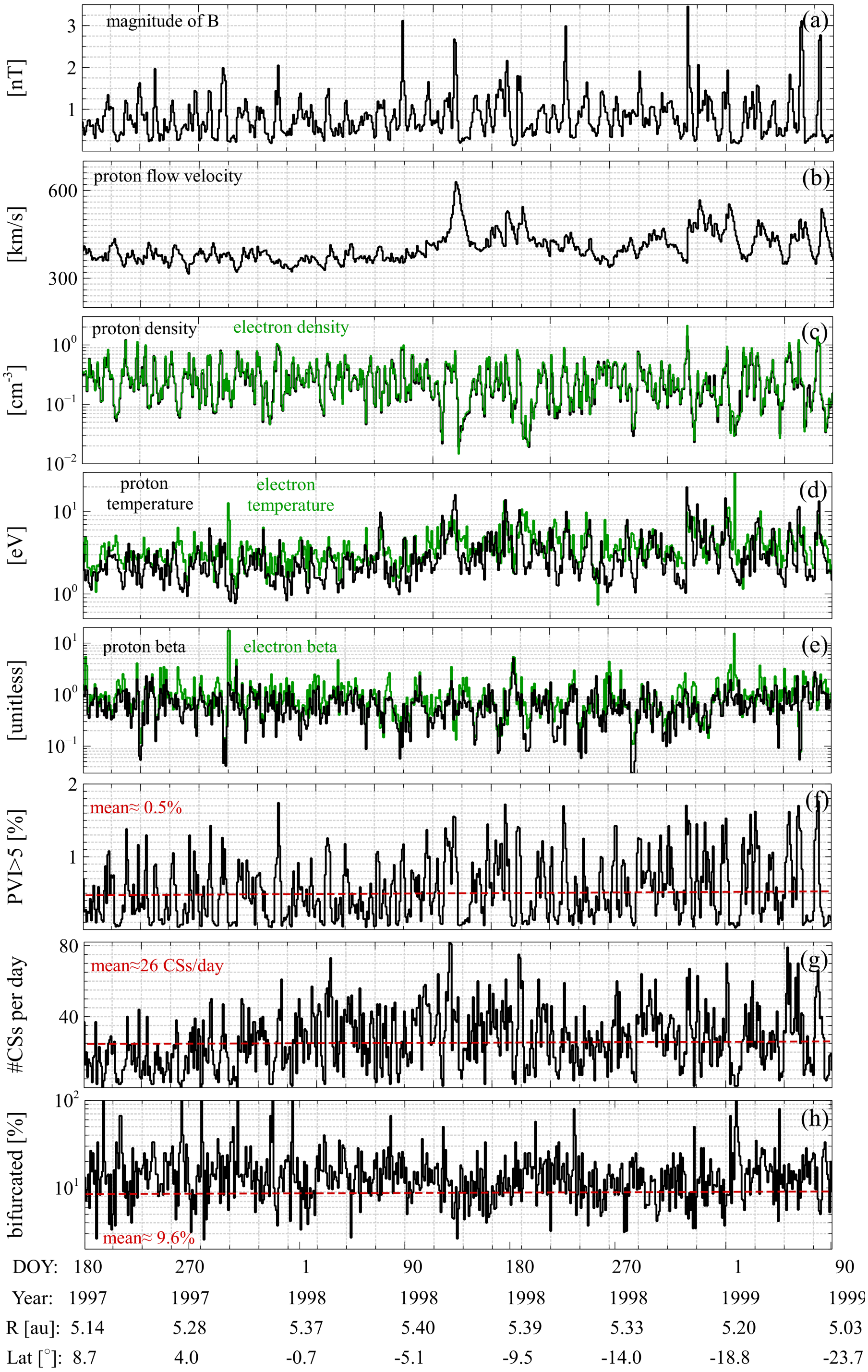

Figure 1. Overview of Ulysses observations over 641 days, from 1997 June 6 to 1999 March 31: (a)–(e) daily averages of the magnetic field magnitude, ion flow velocity, proton and electron densities, temperatures and betas; (f) daily averages of the percentage of data points with the PVI index above the threshold of PVI= 5; (g) the daily occurrence of current sheets and (h) the percentage of current sheets classified as bifurcated. The red lines in panels (f)–(h) represent the averaged values of the corresponding quantities over the 641 days. The labels at the bottom indicate year, DOY (Day Of Year), radial distance and heliographic latitude.

sheet properties will be of value for future comparative analyses of current sheets observed at different radial distances from the Sun.

2 Data and methodology

We consider Ulysses observations over 641 days, from 06/29/1997 to 03/31/1999 that is around solar minimum, when the spacecraft was at about 5 AU and close to the ecliptic plane, at heliographic latitudes within 25°. We use magnetic field measurements provided at the temporal resolution of 1 or 2s by the VHM (Vector Helium Magnetometer) instrument (Balogh et al., 1992), and electron and ion moments (density, flow velocity and temperature) provided at about 6 minute cadence by the SWOOPS (Solar Wind Observations Over the Poles of the Sun) experiment (Bame et al., 1992). While the original magnetic field data had the temporal resolution of 1s for about 70% of data points, we used magnetic field data at 1s resolution obtained by interpolation. The magnetic field is provided in the **RTN** coordinate system, where **R** is along the Sun-spacecraft axis, **T** is the cross product of the solar rotation axis and **R**, and **N** is the cross product of **R** and **T**. Only electron and proton moments are used in this study, while the density of alphas was less then 5% of the ion density for more than 95% of data points and never exceeded 20%. We use the mean of upper and lower estimates of the proton temperature provided by Ulysses, but the presented results would not change if we used the upper or lower estimates instead.

Figure 1 overviews Ulysses observations over the 641 days. Panels (a)–(d) present daily average values of the magnetic field magnitude, ion flow speed, density and temperature of protons and electrons. The magnetic field magnitude was about 0.2–2 nT, the solar wind speed was typically within 450 km/s, electron and proton densities varied between about 0.01 and 1 cm^{-3}, while electron and ion temperatures were mostly within 1–10 eV. Panel (e) shows that electron and proton betas were similar and typically around one. We collected current sheets using the Partial Variance Increments (PVI) methodology (Greco et al., 2008, 2018) previously implemented at 0.2 and 1 AU (Vasko et al., 2021, 2022; Lotekar et al., 2022). In this methodology we compute magnetic field increments $\Delta B_i(t,\tau) = B_i(t+\tau) - B_i(t)$, where the subscript numerates three magnetic field components, while the time lag τ is dictated by data resolution of 1s. Standard deviations σ_i of magnetic field increments are computed every 4 hours, since that is around the correlation scale of turbulence at 5 AU (Smith et al., 2001; Cuesta et al., 2022). We eventually compute the PVI index, $\mathrm{PVI}_\tau(t) = \left[\sum_i \Delta B_i^2/\sigma_i^2\right]^{1/2}$, and identify data points with $\mathrm{PVI}_\tau > 5$. Panel (f) shows that the daily average percentage of such data points substantially varies, while its mean value of 0.5% is four orders of magnitude larger than would be observed if the magnetic field increments had Gaussian probability distributions. The non-Gaussian probability distributions strongly indicate the presence of current sheets and other coherent structures (e.g., Greco et al. (2009, 2018); Matthaeus et al. (2015); Perrone et al. (2017)). We collect current sheets by encompassing each continuous cluster of points with $\mathrm{PVI}_\tau > 5$ by nested intervals up to one minute in duration. If the maximum variance component computed by MVA (Sonnerup & Scheible, 1998) reversed sign within any of the nested intervals, we attempted to manually adjust boundaries to the left and right of the magnetic field reversal. If we could select sufficiently wide boundaries, not shorter than the temporal half-thickness of the reversal, with relatively stable magnetic field, the event was considered a current sheet (CS). Panel (g) shows that the daily average occurrence rate of CSs substantially varies, while the mean value of about 26 CSs/day is similar to the previously reported occurrence rates at 5 AU (Tsurutani et al., 1996; Erdős & Balogh, 2008; Miao et al., 2011). About 9.4% of the CSs were categorized as bifurcated (see below), their daily average occurrence is presented in panel (h). The final dataset includes 16,903 CSs and the corresponding list can be found at Vasko et al. (2024).

Multi-spacecraft observations at 1 AU showed that CSs in the solar wind can be considered locally planar structures frozen into local plasma flow (Burlaga & Ness, 1969; Horbury et al., 2001; Knetter et al., 2004; Wang et al., 2024). These analyses demonstrated that the magnetic field component along the normal to a CS is typically much smaller than local magnetic field magnitude, hardly measurable even using multiple spacecraft. The most accurate single-spacecraft estimate of the normal is therefore delivered by the cross-product of magnetic fields at the CS boundaries (Knetter et al., 2004; Wang et al., 2024). The single-spacecraft methodology based on the cross-product normal and frozen-in assumption used previously for the analysis of magnetic reconnection and CSs at 0.2 and 1 AU (Phan et al., 2010, 2020; Mistry et al., 2017; Vasko et al., 2021; Lotekar et al., 2022; Eriksson et al., 2022) has been recently shown to actually deliver accurate estimates of the CS thickness and current density (Wang et al., 2024). We use this methodology for the CSs observed aboard Ulysses at 5 AU.

Figure 2 demonstrates the application of this methodology for several CSs from our dataset. Panels (a) and (e) present three magnetic field components in the **RTN** coordinate system along with the magnetic field magnitude. Panels (b) and (f) show the same magnetic field in the CS coordinate system $\boldsymbol{xyz}$, where unit vector $\boldsymbol{z}$ is along the cross-product normal, unit vector $\boldsymbol{x}$ is along $\boldsymbol{x}' - \boldsymbol{z} \cdot (\boldsymbol{x}' \cdot \boldsymbol{z})$ with $\boldsymbol{x}'$ being the maximum variance vector determined by MVA, while unit vector $\boldsymbol{y}$ completes the right-handed coordinate system. The maximum variance vector $\boldsymbol{x}'$ is typically almost perpendicular to the cross-product normal and, therefore, vectors $\boldsymbol{x}$ and $\boldsymbol{x}'$ are basically identical (not shown). The normal magnetic field component B_z is by definition zero at the boundaries, but also remains small within the CSs. The CS central region highlighted in the panels corresponds to $|B_x - \langle B_x \rangle| < 0.2\Delta B_x$, where $\langle B_x \rangle$ is the mean of B_x values at the CS boundaries, while ΔB_x is the variation of that component between the boundaries. The assumption that CSs are frozen into local plasma flow allows translating time into space and estimating the current density corresponding to temporal magnetic field gradients: $J_x = (\mu_0 V_n)^{-1} dB_y/dt$ and $J_y = -(\mu_0 V_n)^{-1} dB_x/dt$, where V_n is the normal component of local ion flow velocity that is positive due to appropriate choice of the normal, while $dt = 1$s is dictated by data resolution. Panels (c) and (g) present current density components J_x and J_y, while panels (d) and (h) demonstrate current density components parallel and perpendicular to local magnetic field, $J_{||} = (J_x B_x + J_y B_y)/B$ and $J_\perp = (J_y B_x - J_x B_y)/B$, where B is the magnetic field magnitude. The magnetic field rotation is relatively smooth across the CS in panels (a)–(d), while occurs in two steps for the CS in panels (e)–(h). These CSs exemplify non-bifurcated and bifurcated CSs in our dataset, whose classification was carried out visually.

The adequacy of the visual classification was substantiated *a posteriori* by computing for each CS the cross-correlation coefficient between the observed profile of $J_y(t)$ and a model non-bifurcated profile, $J_{\rm mod}(t) = \langle J_y \rangle \, \mathrm{sech}^2\,(t/\tau_{\rm CS})$, where the brackets denote averaging over the CS central region, $t = 0$ corresponds to the middle of the CS central region, and $\tau_{\rm CS}$ is the temporal half-thickness determined by $\Delta B_x/2\tau_{\rm CS} = \langle dB_x/dt \rangle$. The results of these computations (SM; Supporting Materials) showed that the cross-correlation coefficient is below (above) 0.5 for more than 95% (90%) of the bifurcated (non-bifurcated) CSs, substantiating thereby the adequacy of the visual classification. The temporal scale determined by $\Delta B_x/2\tau_{\rm CS} = \langle dB_x/dt \rangle$ does not necessarily reflect the temporal half-thickness of a bifurcated CS. We determined the temporal half-thickness $\tau_{\rm CS}$ of bifurcated CSs manually as a half of the duration between the middles of the two steps of magnetic field rotation (Figure 2). The spatial half-thickness for both bifurcated and non-bifurcated CSs was computed using the frozen-in assumption, $\lambda = V_n \, \tau_{\rm CS}$.

The non-bifurcated CS shown in Figure 2 is observed at local plasma density of 0.3 cm^{-3}, proton and electron temperatures of 3 eV, and proton and electron betas of $\beta_e \approx \beta_p \approx 1.5$. The local magnetic field magnitude is described by the mean value of magnetic field magnitudes at the CS boundaries, $\langle B \rangle \approx 0.55$ nT. This CS is a proton kinetic-scale structure, since the spatial half-thickness of $\lambda \approx 220$ km is around $0.5\lambda_p$, where λ_p is local proton inertial length. The magnetic field rotates across the CS through shear angle $\Delta\theta \approx 65^\circ$. Since the current density is dominated by the parallel component (Figure

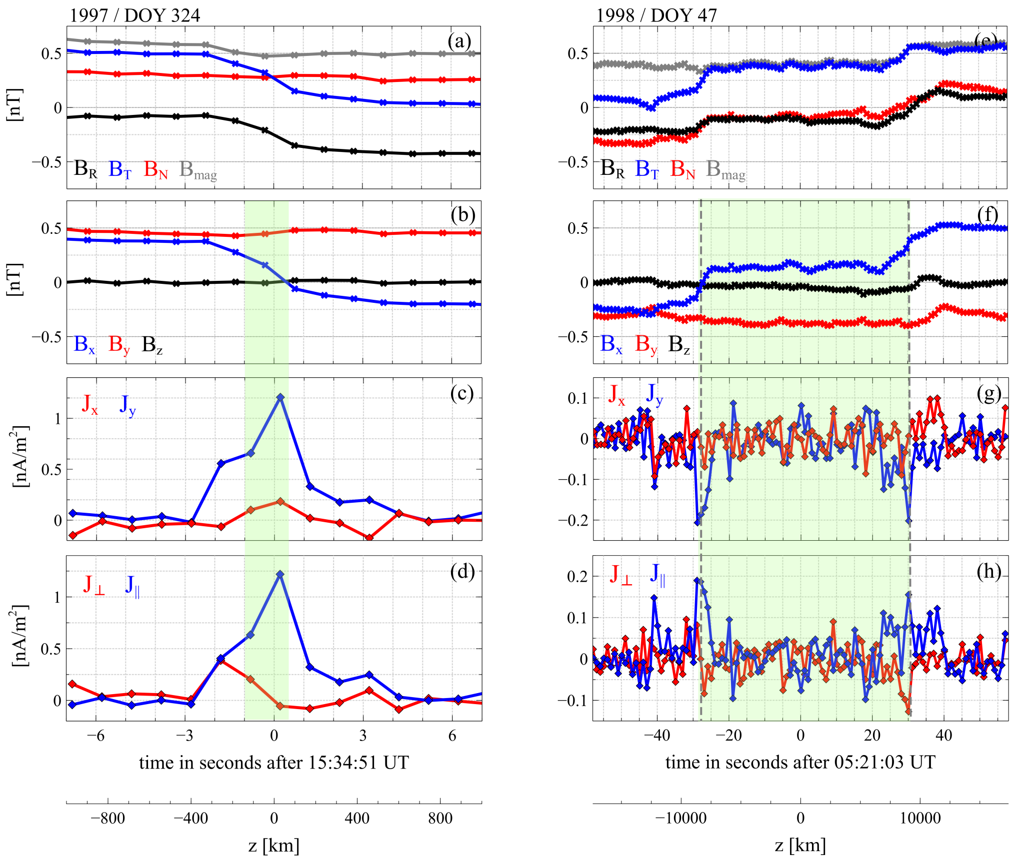

Figure 2. Examples of non-bifurcated (left) and bifurcated (right) current sheets. Panels (a) and (e) show magnetic field magnitude and three magnetic field components in the **RTN** coordinate system. Panels (b) and (f) present three magnetic field components in local coordinate system $\boldsymbol{xyz}$ defined in Section 2. Panels (c) and (g) show current densities J_x and J_y estimated by assuming that current sheets are frozen into local plasma flow: $J_x = (\mu_0 V_n)^{-1} dB_y/dt$ and $J_y = -(\mu_0 V_n)^{-1} dB_x/dt$, where V_n is the normal component of local proton flow velocity, while $dt = 1$s is dictated by data resolution. Panels (d) and (h) present current densities parallel and perpendicular to local magnetic field, $J_{||} = (J_x B_x + J_y B_y)/B$ and $J_\perp = (J_y B_x - J_x B_y)/B$, where B is the magnetic field magnitude. The bottom axes demonstrate the spatial coordinate across each CS, $z = V_n t$ with $t = 0$ corresponding to the middle of the CS central region. The latter are highlighted in the panels and correspond to $|B_x - \langle B_x \rangle| < 0.2\Delta B_x$, where $\langle B_x \rangle$ is the mean of B_x values at the CS boundaries, while ΔB_x is their difference. The dashed gray lines in the left panels indicate the manually determined middles of the two steps of magnetic field rotation for the bifurcated CS.

2), the current density amplitude can be represented by averaged value $J_0 = \langle J_{||} \rangle$ of the parallel current density, and peak value $J_{\rm peak}$ of its magnitude. The observed current density amplitudes of $J_0 \approx 1.1$ nA/m^2 and $J_{\rm peak} \approx 1.2$ nA/m^2 are both close to local Alfvén current density $J_A \approx 1.1$ nA/m^2. Note that $J_A = e n_e V_A$ is the current density corresponding to the drift between electrons and ions of local Alfvén speed, where n_e is local plasma density, $V_A = \langle B \rangle \; (\mu_0 n_e m_p)^{-1/2}$ is local Alfvén speed, e and m_p are the proton charge and mass.

The bifurcated CSs shown in Figure 2 is observed at local plasma density of about 0.5 cm^{-3}, proton and electron temperatures of respectively 0.6 and 1.6 eV, proton and electron betas of $\beta_e \approx 0.8$ and $\beta_p \approx 2$, and local magnetic field magnitude of $\langle B\rangle \approx 0.5$ nT. The spatial half-thickness of the bifurcated CS is $\lambda \approx 8,400$ km that is around $30\lambda_p$ and the magnetic field rotates across the CS through shear angle $\Delta\theta \approx 94^\circ$. For bifurcated CSs we characterize the current density by the peak magnitude $J_{\rm peak}$ of the parallel current density. The observed peak value of $J_{\rm peak} \approx 0.2$ $\mathrm{nA/m^2}$ is around 0.15 J_A. Note that although we presented the spatial scales of both CSs in units of local proton inertial length, similar scales would be observed in units of thermal proton gyroradius $\rho_p = \lambda_p\beta_p^{1/2}$, because proton beta β_p was close to one.

The relative variation of the magnetic field magnitude within both CSs is among the largest in our dataset. The variation of the magnetic field magnitude between the CS boundaries is $\Delta B \approx 0.2\langle B\rangle$ for the non-bifurcated CS and $\Delta B \approx 0.4\langle B\rangle$ for the bifurcated CS. The corresponding maximum variation of the magnetic field magnitude, that is the difference between its maximum and minimum values within CS, is respectively $\Delta B_{\rm max} \approx 0.3\langle B\rangle$ and $0.54\langle B\rangle$. Since the magnitudes of B_y values at the CS boundaries are basically identical (Figure 2), the magnitude variation ΔB is due to different magnitudes of the corresponding B_x values, $\Delta(B^2) \approx \Delta(B_x^2)$ that is equivalent to $\langle B\rangle\Delta B \approx \langle B_x\rangle\Delta B_x$. The relative variation $\Delta B/\langle B\rangle$ critically depends on parameter $\langle B_x\rangle/\Delta B_x$ representing the CS asymmetry. For both CSs presented in Figure 2 the asymmetry parameter was $\langle B_x\rangle/\Delta B_x \approx 0.15$.

Even though challenging to demonstrate experimentally, it is reasonable to assume that solar wind CSs are pressure-balanced structures that is the total of plasma thermal pressure P and magnetic field pressure $B^2/2\mu_0$ remains constant, $2\mu_0 P + B^2 = 2\mu_0 P_0 = \mathrm{const}$ or $2\mu_0 P/B^2 + 1 = 2\mu_0 P_0/B^2$. The latter relation allows estimating the variation of plasma beta between the CS boundaries, $\Delta\beta = 2\mu_0 P_0\ \Delta(B^{-2})$, which will be of value for testing one of the conditions necessary for magnetic reconnection to occur (Swisdak et al., 2003; Swisdak et al., 2010; Phan et al., 2010). The mean of the pressure balance relation at the CS boundaries allows excluding P_0 and revealing that

$$\Delta\beta = (1+\beta)\Delta(B^{-2})/\langle B^{-2}\rangle, \tag{1}$$

where $\beta \equiv \langle 2\mu_0 P/B^2\rangle = (2\mu_0\langle P\rangle + \langle B^2\rangle)\langle B^{-2}\rangle - 1$ is the mean of plasma beta values at the boundaries (Vasko et al., 2021). We estimated β by assuming that the plasma pressure observed aboard Ulysses at the temporal resolution of about 6 minutes adequately reflects the mean $\langle P\rangle$ of plasma pressure values at the boundaries. For the CSs shown in Figure 2 we found $\beta \approx 3.2$ and $\Delta\beta \approx 1.8$ for the non-bifurcated CS, and $\beta \approx 3.3$ and $\Delta\beta \approx 3.4$ for the bifurcated CS.

The presented analysis was carried out for all the 16,903 collected CSs, including 15,309 non-bifurcated and 1,594 bifurcated CSs. Note that bifurcated magnetic field profile does not necessarily imply magnetic reconnection (Gosling & Szabo, 2008; Phan et al., 2020) and we are not able to determine the fraction of reconnecting CSs in our dataset because of the low temporal resolution of plasma measurements. For each CS in our dataset we determined shear angle, half-thickness, current density amplitudes, and quantities characterizing the CS asymmetry and magnetic field magnitude variation within CS. The statistical distributions of these parameters are presented in the next section. The half-thickness and current density amplitudes are compared to local proton inertial length and Alfvén current density, that is the Alfvén units typically used in turbulence simulations (e.g., Zhdankin et al. (2013); Franci et al. (2017); Papini et al. (2019); Jain et al. (2021)). We complete this section by pointing out that local magnetic field of solar wind CSs can be described by a universal one-dimensional model

$$\mathbf{B} = B(z)\sin\theta(z)\ \boldsymbol{x} + B(z)\cos\theta(z)\ \boldsymbol{y} + B_z\boldsymbol{z},$$

where $B(z)$ and $\theta(z)$ determine spatial profiles of magnetic field magnitude and rotation, while B_z is equal or close to zero, $B_z \ll B$. The current density components parallel and

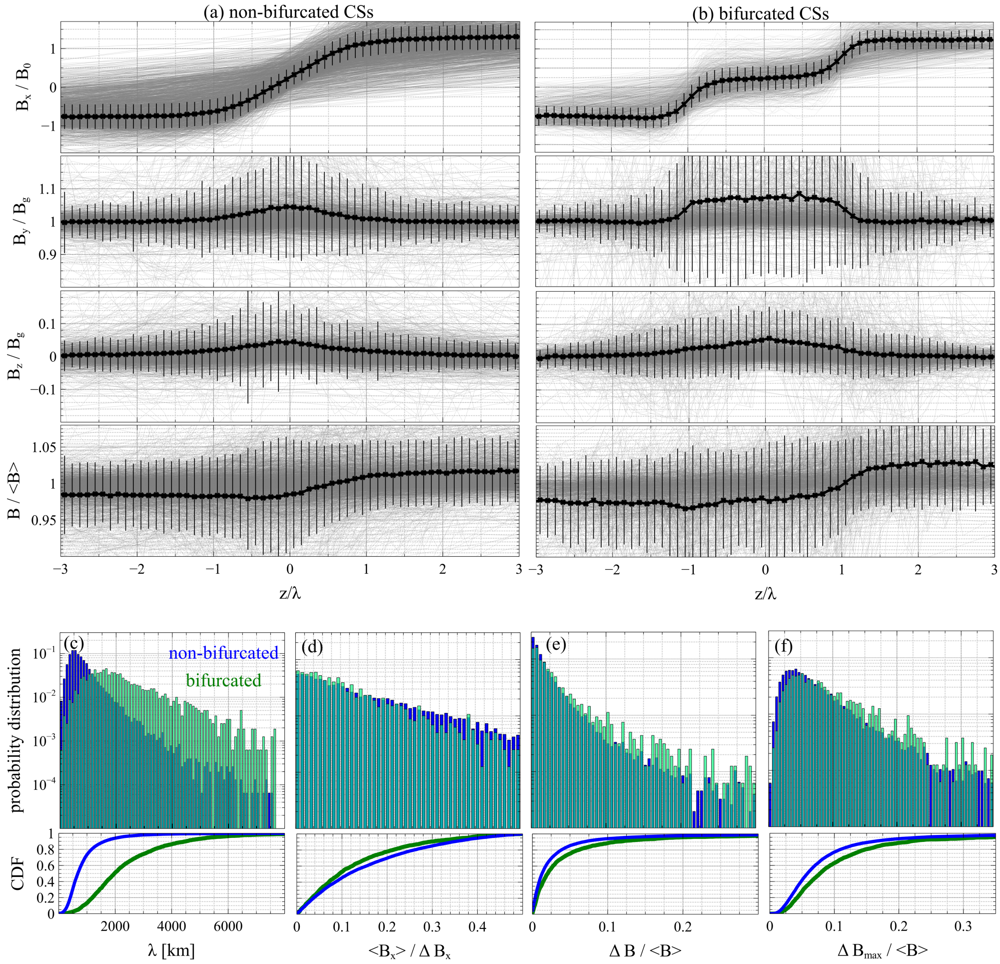

Figure 3. Averaged (black) and individual (gray) magnetic field profiles of (a) non-bifurcated and (b) bifurcated CSs. Before averaging, individual profiles were first aligned by setting $z = 0$ in the middle of the CS central region and normalizing the spatial coordinate to the CS half-thickness, $z \rightarrow z/\lambda$. Individual profiles of B_x were then normalized to $B_0 = 0.5\Delta B_x$ that is a half of the difference between B_x values at the CS boundaries. Individual profiles of B_y and B_z were normalized to guide field B_g that is the mean of B_y values at the CS boundaries. Individual profiles of magnetic field magnitude B were normalized to $\langle B\rangle$ that is the mean of magnetic field magnitudes at the CS boundaries. The error bars in panels (a) and (b) indicate standard deviations. Panels (c)–(f) present probability and corresponding cumulative distributions of the CS half-thickness λ, parameter $\langle B_x\rangle/\Delta B_x$ quantifying the CS asymmetry, and parameters $\Delta B/\langle B\rangle$ and $\Delta B_{\max}/\langle B\rangle$ quantifying the relative variation of the magnetic field magnitude between the CS boundaries and within CS.

perpendicular to local magnetic field are solely determined by magnetic field rotation and magnitude variation

$$J_{\parallel} = (B/\mu_0)\, d\theta/dz, \quad J_{\perp} = (1/\mu_0)\, dB/dz \tag{2}$$

By the order of magnitude we have

$$J_{\perp}/J_{\parallel} \approx \Delta B/\langle B\rangle\Delta\theta \tag{3}$$

and use this parameter in the next section to quantify the ratio between average values of the perpendicular and parallel current densities.

3 Statistical results

3.1 Current sheet properties and scale-invariance

We determine typical magnetic field profiles of bifurcated and non-bifurcated CSs by averaging appropriately aligned and normalized magnetic field profiles of the collected CSs. The individual magnetic field profiles were aligned by setting the CS center, where $B_x = \langle B_x \rangle$, at $z = 0$ and normalizing the spatial coordinate to the CS half-thickness, $z \to z/\lambda$. For bifurcated CSs the center was set in the middle between the two steps of magnetic field rotation, since we typically had $B_x \approx \langle B_x \rangle$ over the entire plateau in between the steps. Each individual profile of magnetic field magnitude B and guide field component B_y was normalized to the mean of their values at the CS boundaries. The mean guide field B_g was also used to normalize the corresponding B_z profile. Each profile of B_z/B_g was also multiplied by its sign at the CS center, so that the averaged profile could reveal the magnitude of B_z/B_g around the CS central region. The individual B_x profiles were normalized to $B_0 = \Delta B_x/2$ that is a signed quantity representing the variation of B_x between the CS boundaries. Note that B_x/B_0 always varies from a negative value at the left boundary to a positive value at the right boundary. Each profile of B_x/B_0 with a smaller magnitude at the right boundary was reflected with respect the CS center and multiplied by -1 to always have the smaller magnitude of B_x/B_0 at the left boundary. If the reflection was required for a B_x/B_0 profile, it was also performed for other corresponding magnetic field profiles. The reflection procedure was necessary to reveal the asymmetry typical of the CSs in the averaged profiles.

Figure 3 presents the averaged magnetic field profiles along with the profiles of individual CSs. The averaged profiles in panels (a) and (b) clearly demonstrate that magnetic field rotation occurs smoothly across non-bifurcated CSs, while in two steps across bifurcated CSs. The averaged B_x/B_0 profiles show that both types of CSs are typically asymmetric with the left and right boundary values of about -0.75 and 1.25, respectively. In contrast, the guide field typically has identical boundary values according to the averaged B_y/B_g profiles and increases by about 10% toward the CS central region. The normal component is by definition close to zero at the boundaries, while also remains small, less than about $0.1B_g$, within CS. The averaged profiles of $B/\langle B \rangle$ show that the boundary values of the magnetic field magnitude differ by a few percent, which is due to statistically different magnitudes of B_x values at the boundaries, $\Delta B^2 = \Delta(B_x^2) + \Delta(B_y^2) \approx \Delta(B_x^2)$ that is equivalent to $\langle B \rangle \Delta B \approx \langle B_x \rangle \Delta B_x$. The probability and corresponding cumulative distributions in panel (c) demonstrate that bifurcated CSs are statistically wider than non-bifurcated CSs. The corresponding median values of the CS half-thickness are around 700 and 2,000 km, while the scales of both types of CSs range from a few tens to 10,000 km. The statistical distributions in panels (d)–(f) demonstrate that bifurcated and non-bifurcated CSs have more or less similar asymmetry and variations of the magnetic field magnitude. Both types of CSs are typically asymmetric with $\langle B_x \rangle/\Delta B_x \gtrsim 0.1$ for more than 50% of the CSs. The magnetic field magnitude does not substantially vary within the CSs, since for more than 90% of the CSs we have $\Delta B/\langle B \rangle \lesssim 0.1$ for the variation of the magnetic field magnitude between the CS boundaries and $\Delta B_{\max}/\langle B \rangle \lesssim 0.2$ for the maximum variation.

Figure 4 demonstrates that some of the CS parameters depend on local plasma beta β. Panels (a) and (b) present probability and cumulative distributions of $\Delta B/\langle B \rangle$ and $\Delta B_{\max}/\langle B \rangle$ for 5,197 CSs observed at $\beta < 1$ and 4,238 CSs observed at $\beta > 3$. The distributions demonstrate that larger variations of the magnetic field magnitude are typical at lager betas. Panel (c) presents corresponding statistical distributions of parameter $\Delta B/\langle B \rangle \Delta\theta$ quantifying the ratio between average values of the parallel and perpendicular current density according to Eq. (3). The distributions demonstrate that the current den-

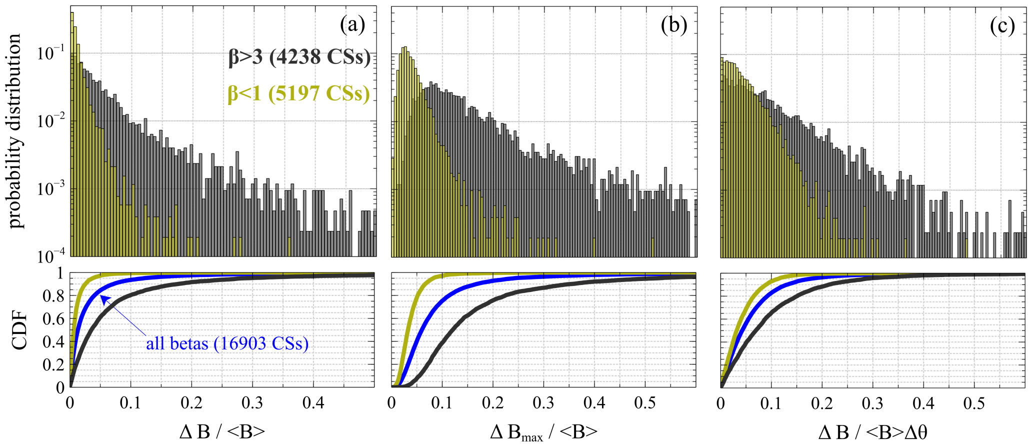

Figure 4. Probability and cumulative distributions of parameters $\Delta B/\langle B\rangle$, $\Delta B_{\rm max}/\langle B\rangle$ and $\Delta B/\langle B\rangle\Delta\theta$ for subsets of the CSs observed at different plasma betas, $\beta<1$ and $\beta>3$. The bottom panels also present the cumulative distributions corresponding to all the CSs in our dataset. Note that according to Eq.(3) parameter $\Delta B/\langle B\rangle\Delta\theta$ quantifies the ratio between average perpendicular and parallel current densities within CS.

sity in the CSs is typically dominated by the parallel component, $\Delta B/\langle B\rangle\Delta\theta\lesssim 0.1$ for more than about 90% of the CSs, but the relative magnitude of the perpendicular current density tends to be larger at larger betas. The scatter plots between local beta and the considered CS parameters also demonstrate positive correlation (SM).

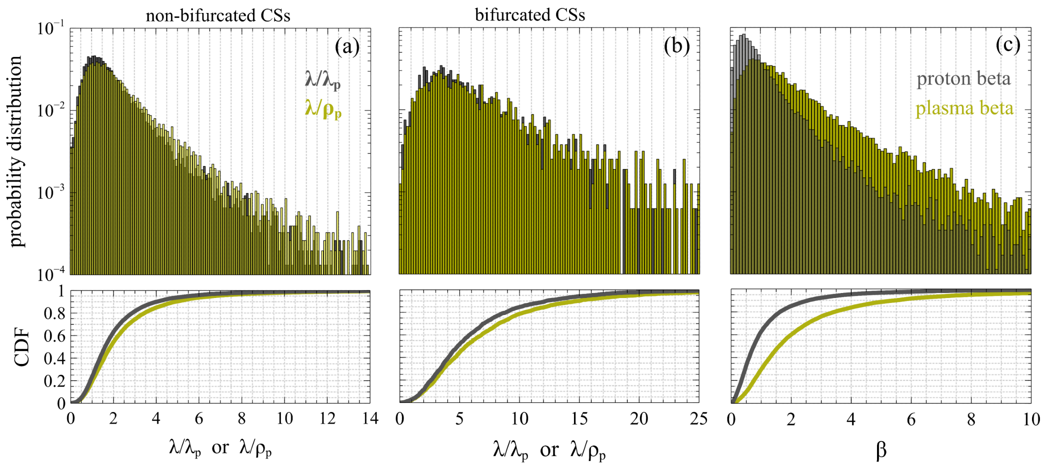

Figure 5. Panels (a) and (b) present probability and cumulative distributions of the half-thickness of non-bifurcated and bifurcated CSs in units of local proton inertial length λ_p and thermal proton gyroradius ρ_p. Panel (c) presents probability and cumulative distributions of proton beta and total plasma beta corresponding to the CSs in our dataset.

Figure 5 presents the half-thickness of the CSs in units of proton inertial length λ_p and thermal proton gyroradius $\rho_p=\lambda_p\beta_p^{1/2}$. The probability and cumulative distributions in panels (a) and (b) show that both types of CSs are typically proton kinetic-scale structures. For non-bifurcated CSs the median value of the half-thickness is about $1.5\lambda_p$, the corresponding 5th and 95th percentiles are respectively around 0.5 and $5\lambda_p$. For bifurcated CSs the median value is around $5\lambda_p$, while the 5th and 95th percentiles are about 0.7 and $15\lambda_p$. We observe similar spatial scales in units of thermal proton gyroradius, because proton beta β_p was typically around one. Panel (c) shows that the median value of proton beta is about 0.7, while the 5th and 95th percentiles are respectively about 0.15 and 3. Note that electron and proton betas had almost identical probability distributions (SM), while in panel (c) we show the statistical distribution of total plasma beta, $\beta = \beta_p + \beta_e$.

Figure 6 demonstrates statistical distributions of amplitudes of the parallel current density observed within the CSs. Panel (a) shows that the averaged and peak amplitudes, J_0 and $J_{\rm peak}$, have basically identical statistical distributions. The median value of both current density amplitudes is around 0.15 nA/m^2, while the 5th and 95th percentiles are about 0.05 and 0.5 nA/m^2. The statistical distributions in panel (b) demonstrate that in units of local Alfvén current density the observed current density amplitudes have the median value of about $0.1J_A$, while the 5th and 95th percentiles are about 0.04 and $0.4J_A$. Panel (c) shows that independent of the type of CSs, the peak current density $J_{\rm peak}$ is strongly correlated with local Alfvén current density J_A, which varies in our dataset from 0.1 to 10 nA/m^2. Similar strong correlation is observed between J_0 and J_A (not shown).

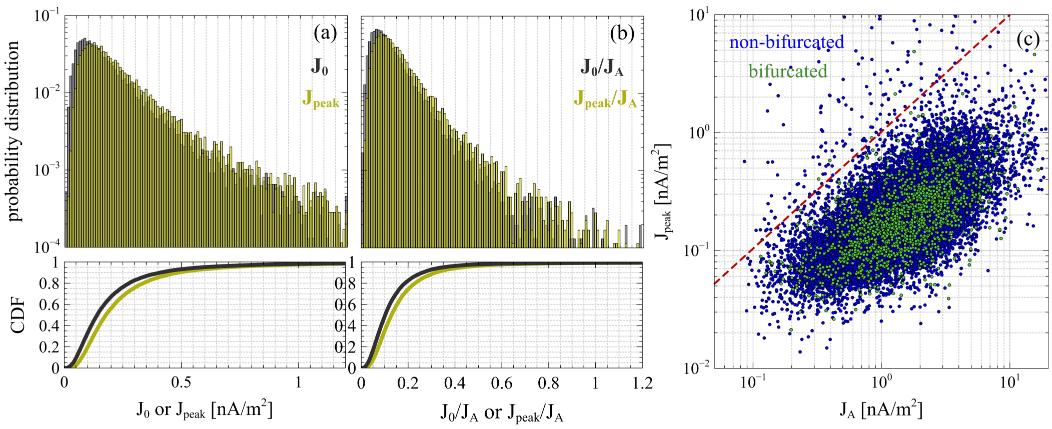

Figure 6. Panel (a) presents probability and cumulative distributions of the peak value $J_{\rm peak}$ of the parallel current density within CS and the current density amplitude J_0 averaged over the CS central region. Note that the averaged amplitude J_0 was computed only for non-bifurcated CSs, while $J_{\rm peak}$ was computed for both types of CSs. Panel (b) shows probability and cumulative distributions of the current density amplitudes normalized to local Alfvén current density J_A. Panel (c) demonstrates a scatter plot between current density amplitude $J_{\rm peak}$ and local Alfvén current density J_A for bifurcated (green) and non-bifurcated (blue) CSs. The red line in panel (c) corresponds to equality of the two quantities.

Figure 7 shows that to some extent the CSs exhibit scale-invariance that is several of the CS parameters depend on their spatial scale in a power law fashion. The scatter plots in panels (a)–(c) demonstrate that the shear angle as well as the normalized magnetic field and current density amplitudes are correlated with the CS half-thickness normalized to proton inertial length. The correlation can be quantified by fitting scattered data to a power law as well as binning the data as shown in panel (d) and computing the median value of a considered CS parameter within each bin. We also computed the 15th and 85th percentiles within each bin to demonstrate, where 70% of the CSs resides. The median profiles in panels

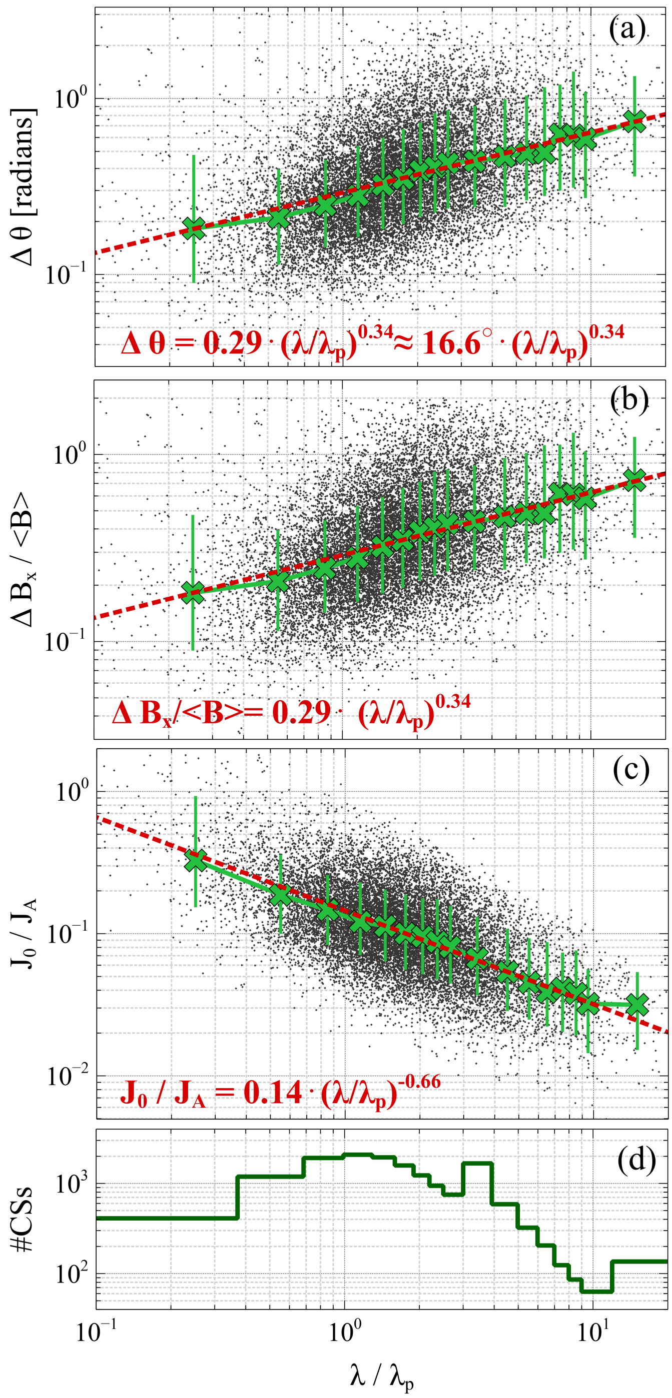

Figure 7. Scatter plots of normalized half-thickness λ/λ_p versus (a) magnetic shear angle $\Delta\theta$, (b) normalized magnetic field amplitude $\Delta B_x/\langle B\rangle$ and (c) normalized current density J_0/J_A. These scatter plots were produced for non-bifurcated CSs, since the averaged value J_0 only reflects the current density amplitude of non-bifurcated CSs. The non-bifurcated CSs were sorted into bins corresponding to different values of the normalized half-thickness and median values of the quantities shown in panels (a)–(c) were computed within each bin. The number of CSs within each bin is shown in panel (d). Panels (a)–(c) present the median profiles (green curves) along with error bars indicating the 15th and 85th percentiles within each bin. The panels also present the best power law fits of the scattered data (red curves) along with the best fit parameters.

(a)–(c) demonstrate that shear angle $\Delta\theta$ and magnetic field amplitude $\Delta B_x/\langle B\rangle$ tend to increase with increasing spatial scale, while, in contrast, current density amplitude J_0/J_A increases with decreasing spatial scale. The same trends are revealed by the best power law fits

$$\Delta\theta \approx 16.6^\circ(\lambda/\lambda_p)^{0.34}, \quad \Delta B_x/\langle B\rangle \approx 0.29\,(\lambda/\lambda_p)^{0.34}, \quad J_0/J_A \approx 0.14\,(\lambda/\lambda_p)^{-0.66}. \tag{4}$$

Note that the scale-dependencies of $\Delta\theta$ and $\Delta B_x/\langle B\rangle$ are basically equivalent, because in the case of CSs with moderate asymmetry and relatively constant magnetic field magnitude (Figure 3) we have $\Delta B_x \approx 2\langle B\rangle\sin(\Delta\theta/2)$ that is approximately equivalent to $\Delta B_x/\langle B\rangle \approx \Delta\theta$. The scale-dependence of the current density amplitude could be also deduced from the scale-dependence of the shear angle, because according to Eq. (2) we have $J_0 \approx \langle B\rangle\Delta\theta/2\mu_0\lambda$ that is equivalent to $J_0/J_A \approx \Delta\theta\ (2\lambda/\lambda_p)^{-1}$. In the next section we match the scale-dependence of the shear angle against the scale-dependence of all magnetic field rotations in ambient solar wind.

3.2 Current sheets versus turbulence properties

We quantify the properties of all magnetic field fluctuations in ambient solar wind by computing at each moment of time the angle α_τ between magnetic field vectors separated by time lag τ

$$\alpha_\tau(t) = \cos^{-1}\left[\frac{\mathbf{B}(t+\tau)\cdot\mathbf{B}(t)}{B(t+\tau)B(t)}\right] \tag{5}$$

At each moment of time we also compute parameter χ_τ characterizing the compressibility of magnetic field fluctuations

$$\chi_\tau(t) = \frac{\delta b_\tau - 2\sin(\alpha_\tau/2)}{\delta b_\tau}, \quad \delta b_\tau = \frac{|\mathbf{B}(t+\tau)-\mathbf{B}(t)|}{\langle B\rangle_\tau}, \tag{6}$$

where $\langle B\rangle_\tau \equiv (B(t+\tau)+B(t))/2$. Note that $\chi_\tau \in [0,1]$ with $\chi_\tau = 0$ corresponding to purely incompressible fluctuations (magnetic field rotations), and $\chi_\tau = 1$ corresponding to purely compressible fluctuations (magnitude variations of a unidirectional magnetic field). The statistical properties of parameters α_τ and χ_τ were previously addressed for magnetic field fluctuations at 1 AU (Zhdankin et al., 2012; Chen et al., 2015). In this section not only do we present similar analysis of magnetic field fluctuations observed aboard Ulysses over the 641 days, but also match statistical properties of parameters α_τ and χ_τ against equivalent CS parameters. The latter include shear angle $\Delta\theta$ and parameter $\chi^{\rm b}_{\rm CS}$ computed using Eq. (6) for magnetic fields at the CS boundaries. Parameter $\chi^{\rm b}_{\rm CS}$ characterizes the magnetic field compressibility between CS boundaries and can be expressed through previously introduced quantities

$$\chi^{\rm b}_{\rm CS} = \frac{(1+\xi^2)^{1/2}-1}{(1+\xi^2)^{1/2}}, \qquad \xi \equiv \frac{\Delta B\cos(\Delta\theta/2)}{2\langle B\rangle\sin(\Delta\theta/2)}. \tag{7}$$

Since typically $\xi \approx \Delta B/\langle B\rangle\Delta\theta$ and $\xi \ll 1$ (Figure 4), we have $\chi^{\rm b}_{\rm CS} \approx 0.5(\Delta B/\langle B\rangle\Delta\theta)^2$ that is also equivalent to $\chi^{\rm b}_{\rm CS} \approx 0.5(J_\perp/J_\parallel)^2$ according to Eq. (3). We also apply Eq. (6) to compute parameter $\chi^{\rm max}_{\rm CS}$ for magnetic fields $\mathbf{B}_{\rm min}$ and $\mathbf{B}_{\rm max}$ corresponding to the minimum and maximum magnetic field magnitudes within CS. This parameter is a measure of the maximum compressibility within CS and can be expressed through Eq. (7) with appropriate replacements, $\Delta B \to \Delta B_{\rm max}$, $\langle B\rangle \to (B_{\rm min}+B_{\rm max})/2$ and $\Delta\theta \to \cos^{-1}(\mathbf{B}_{\rm min}\cdot\mathbf{B}_{\rm max}/B_{\rm min}B_{\rm max})$.

Figure 8 presents statistical properties of magnetic field rotation angles α_τ for a broad range of time lags, $\tau = $ 1–300s. Probability density functions (PDFs) of α_τ shown in panel (a) demonstrate that smaller rotation angles are typical at smaller time lags. For each time lag τ we computed the mean rotation angle $\langle\alpha_\tau\rangle$ and PDFs of $\alpha_\tau/\langle\alpha_\tau\rangle$ shown in panel (b).

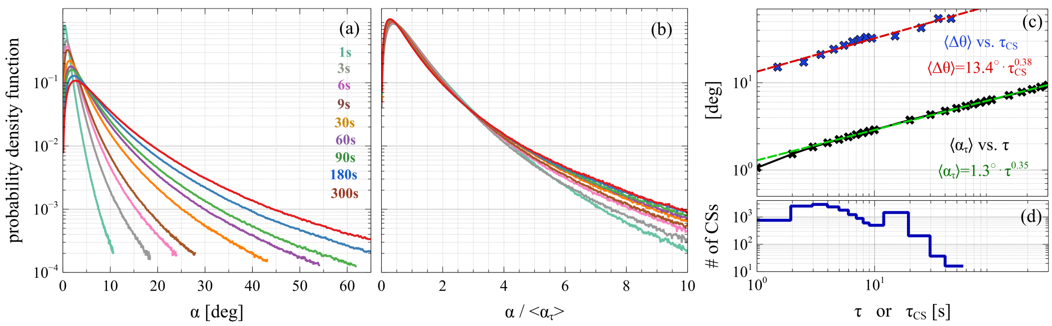

Figure 8. The analysis of magnetic field rotation angles across all magnetic field fluctuations observed over the considered 641 days: (a) probability density functions of magnetic field rotation angles α_τ at temporal scale τ that was varied between 1 and 300s (Eq. (5)); (b) probability density functions of α_τ normalized to mean rotation angle $\langle \alpha_\tau \rangle$ at scale τ; (c) the mean rotation angle $\langle \alpha_\tau \rangle$ versus τ along with the best power law fit (green). Panel (c) also presents the mean shear angle $\langle \Delta\theta \rangle$ versus CS temporal scale, obtained by binning the CSs by temporal half-thickness $\tau_{\rm CS}$ as shown in panel (d). The red line shows the best power law fit to the observed trend of larger $\langle \Delta\theta \rangle$ for larger $\tau_{\rm CS}$.

The latter PDFs practically collapsed to a universal distribution, indicating thereby that magnetic field fluctuations of different temporal scales observed aboard Ulysses are to some extent self-similar. Similar self-similarity was previously reported for magnetic field rotations at 1 AU (Zhdankin et al., 2012; Chen et al., 2015). In panel (c) we match the properties of rotation angles across the CSs and all the magnetic field fluctuations. Panel (c) demonstrates that the mean rotation angle $\langle \alpha_\tau \rangle$ scales with the time lag, $\langle \alpha_\tau \rangle \approx 1.3^\circ \tau^{0.35}$, though a slight deviation off that scaling is observed at $\tau \approx 1$s. We computed the mean shear angle $\langle \Delta\theta \rangle$ for CSs of different temporal scales by binning the CSs according to their temporal half-thickness $\tau_{\rm CS}$, which varies from about 1 to 60s according to panel (d). The best power law fit to the trend revealed by the bin-averaging, $\langle \Delta\theta \rangle \approx 13.4^\circ \tau_{\rm CS}^{0.38} \approx 10.3^\circ\,(2\tau_{\rm CS})^{0.38}$, is practically identical to the scaling followed by all the magnetic field rotations in the solar wind, except that the mean shear angle is much larger, because CSs are the largest magnetic field rotations at any given scale. Note that the scaling relation involving $2\tau_{\rm CS}$ reflects that $\Delta\theta$ is the angle between magnetic fields at the CS boundaries separated by roughly $2\tau_{\rm CS}$.

Figure 9 matches the magnetic field compressibility within the CSs against all magnetic field fluctuations in ambient solar wind. Panel (a) presents PDFs of χ_τ computed for $\tau =$ 1–300s, while corresponding cumulative distributions are shown in panel (b). The magnetic field fluctuations at smaller temporal scales tend to have higher compressibility that is larger relative variations of the magnetic field magnitude. The higher compressibility at smaller scales was previously reported for magnetic field fluctuations at 1 AU (Hamilton et al., 2008; Podesta, 2009; Chen et al., 2015). Panels (c) and (d) present PDFs and cumulative distributions of parameters $\chi_{\rm CS}^{\rm b}$ and $\chi_{\rm CS}^{\rm max}$. Since the CSs have temporal half-thickness $\tau_{\rm CS}$ from about 1 to 60s, we also duplicate in panels (c) and (d) the statistical distributions of χ_τ for $\tau = 1$ and 60s. The compressibility between the CS boundaries quantified by parameter $\chi_{\rm CS}^{\rm b}$ is much smaller than typical compressibility of ambient magnetic field fluctuations at comparable temporal scales. In quite a contrast, the maximum compressibility within CS quantified by parameter $\chi_{\rm CS}^{\rm max}$ is practically identical to that of the ambient fluctuations. Panel (e) presents mean value $\langle \chi_\tau \rangle$ versus τ as well as mean values of $\chi_{\rm CS}^{\rm b}$ and $\chi_{\rm CS}^{\rm max}$ computed by binning the CSs by their temporal half-thickness $\tau_{\rm CS}$ as shown in panel (f). All the mean values of compressibility increase toward smaller scales and we also observe $\langle \chi_{\rm CS}^{\rm b} \rangle \ll \langle \chi_\tau \rangle$

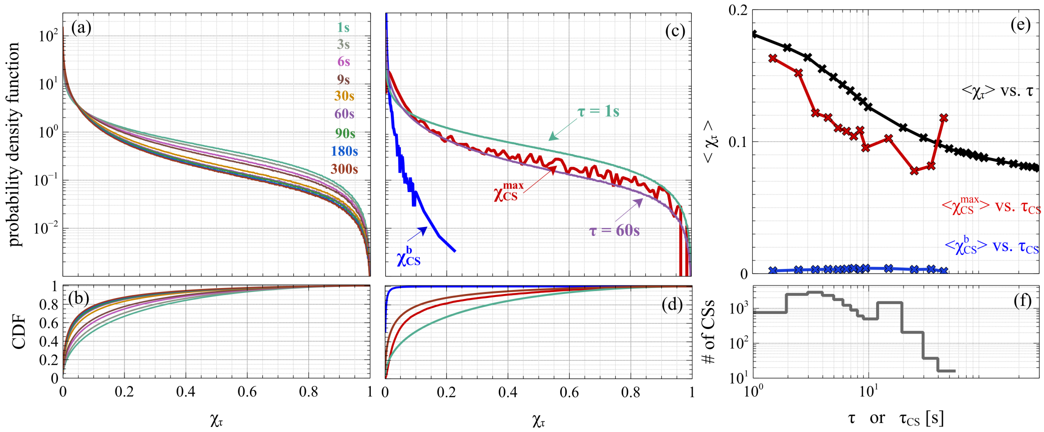

Figure 9. The analysis of compressibility of all magnetic field fluctuations observed over the considered 641 days. The compressibility of fluctuations at temporal scale τ is quantified by parameter $\chi_\tau \in [0,1]$ defined by Eq. (6) with $\chi_\tau = 0$ and $\chi_\tau = 1$ corresponding respectively to purely incompressible (magnetic field rotations) and compressible (magnitude variations of a unidirectional magnetic field) fluctuations. Panels (a) and (b) present probability density functions and corresponding cumulative distributions of parameter χ_τ at temporal scales τ between 1 and 300s. Panels (c) and (d) duplicate the latter distributions for $\tau = 1$ and 60s along with distributions of parameters $\chi^{\rm b}_{\rm CS}$ and $\chi^{\rm max}_{\rm CS}$ quantifying magnetic field compressibility within the CSs (Eq. (7)). Panel (e) presents mean compressibility $\langle\chi_\tau\rangle$ versus τ along with mean values $\langle\chi^{\rm b}_{\rm CS}\rangle$ and $\langle\chi^{\rm max}_{\rm CS}\rangle$ of magnetic field compressibility observed within CSs of different scales, obtained by binning the CSs by their temporal half-thickness $\tau_{\rm CS}$ as shown in panel (f).

and $\langle\chi^{\rm b}_{\rm CS}\rangle \ll \langle\chi^{\rm max}_{\rm CS}\rangle$. Note that $\langle\chi^{\rm b}_{\rm CS}\rangle$ is around 10^{-3}, which is consistent with the fact that $\chi^{\rm b}_{\rm CS} \approx 0.5(\Delta B/\langle B\rangle\Delta\theta)^2$ and typical values of $\Delta B/\langle B\rangle\Delta\theta$ (Figure 4). Thus, the maximum compressibility within the CSs is basically identical to that of ambient magnetic field fluctuations at comparable temporal scales, while the compressibility computed between the CS boundaries is about two orders of magnitudes lower.

3.3 Current sheets and magnetic reconnection

The collected CSs have the typical temporal scale from about 1 to 60s. In turn, the temporal resolution of plasma measurements aboard Ulysses is only around 6 minutes, which implies magnetic reconnecting cannot be identified by resolving plasma jets potentially present within the CSs. We can however test one of the theoretical conditions necessary for magnetic reconnection to occur. Swisdak et al. (2010) showed that magnetic reconnection is suppressed in the case of a sufficiently high CS asymmetry, $\Delta\beta \gtrsim 2(L/\lambda_p)\tan(\Delta\theta/2)$, where $\Delta\beta$ is the plasma beta variation between the CS boundaries, $\Delta\theta$ is the shear angle, while parameter L/λ_p is of the order of one and represents the typical scale of plasma pressure gradient across X-line.

Figure 10 presents the test of this condition for both bifurcated and non-bifurcated CSs with the plasma beta variation $\Delta\beta$ estimated by Eq. (1). Panels (a) and (b) show that independent of the type, most of the CSs are in the parameter range, where reconnection cannot be suppressed due to the asymmetry. For both types of CSs we have only about 11% and 5% of the CSs with $\Delta\beta \gtrsim 2(L/\lambda_p)\tan(\Delta\theta/2)$ for $L/\lambda_p = 1$ and $L/\lambda_p = 2$, respectively. Panel (c) matches $\Delta\beta$ against $2(\lambda/\lambda_p)\tan(\Delta\theta/2)$, testing thereby the same condition with parameter L equal to the observed CS half-thickness λ. We have only about 7% of the

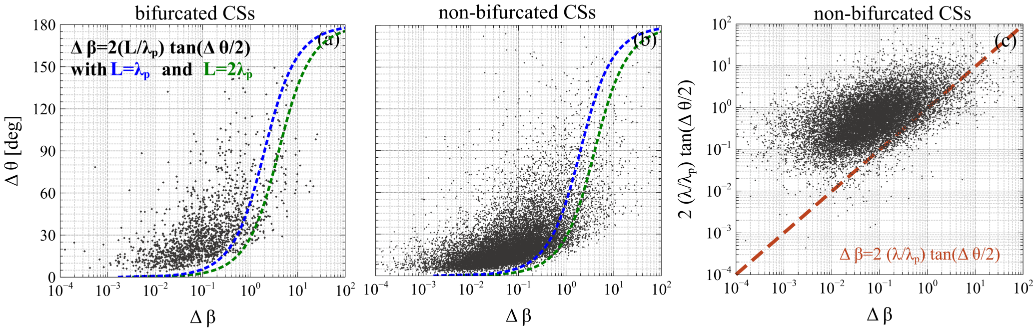

Figure 10. Testing of the suppression condition of magnetic reconnection through the diamagnetic drift of X-line (Section 3.3). Magnetic reconnection is suppressed, when the difference $\Delta\beta$ of plasma betas at the CS boundaries is sufficiently large, $\Delta\beta \gtrsim 2(L/\lambda_p)\tan(\Delta\theta/2)$, where L/λ_p is of the order of one. Panels (a) and (b) present the test of the suppression condition with $L/\lambda_p = 1$ and 2 for bifurcated and non-bifurcated CSs, while panel (c) presents the test of this condition with $L = \lambda$.

CSs with $\Delta\beta \gtrsim 2(\lambda/\lambda_p)\tan(\Delta\theta/2)$. This analysis demonstrates that for most of the CSs magnetic reconnection cannot be suppressed by the asymmetry and is, in principle, allowed if not suppressed by other processes.

4 Discussion

Solar wind CSs were observed at 0.3–8 AU and 20 AU aboard early spacecraft missions (Burlaga, 1969; Mariani et al., 1973; Burlaga et al., 1977; Tsurutani & Smith, 1979; Lepping & Behannon, 1986; Söding et al., 2001). The selection procedures implemented in the early studies were based on magnetic field data of relatively low temporal resolution and were naturally biased toward large scale CSs. The high-resolution magnetic field measurements aboard modern spacecraft missions demonstrated that CSs are much more abundant and statistically thinner than reported early on (Vasquez et al., 2007; Perri et al., 2012; Podesta, 2017; Artemyev, Angelopoulos, & Vasko, 2019; Vasko et al., 2021, 2022; Lotekar et al., 2022; Wang et al., 2023). The CSs were also shown to substantially contribute into magnetic field spectra of solar wind turbulence (Borovsky & Podesta, 2015; Borovsky & Burkholder, 2020) and potentially cause plasma heating (Osman et al., 2012; Wu et al., 2013; Qudsi et al., 2020; Sioulas et al., 2022). There are several comprehensive analyses of solar wind CSs at 0.2 and 1 AU, but only few analyses of similar structures at the distances well beyond 1 AU. The results of previous studies of CSs at 5 AU are highly valuable (Tsurutani et al., 1996; Erdős & Balogh, 2008; Miao et al., 2011), but insufficient for matching against the recent results reported at 0.2 and 1 AU (Vasko et al., 2021, 2022; Lotekar et al., 2022).

We presented the analysis of 16,903 CSs collected over 641 days of Ulysses observations at 5 AU near the ecliptic plane and close to solar minimum. The revealed occurrence rate of 26 CSs/day is close to occurrence rates of 15–25 CSs/day observed previously aboard Ulysses at 5 AU (Tsurutani et al., 1996; Erdős & Balogh, 2008; Miao et al., 2011). The CSs in our dataset have temporal half-thickness $\tau_{\rm CS}$ between about 1 and 60s, which is similar to temporal scales reported by Miao et al. (2011) and Tsurutani et al. (1996). Note that our dataset contains small scale CSs not captured by Erdős and Balogh (2008), whose dataset included CSs with scales larger than 1,000 km, probably because CSs were selected using magnetic field data downsampled to 10s. The averaged profiles in Figure 3 demonstrate that the magnetic field rotates across CS, while remains almost constant in magnitude in accordance with previous observations (Tsurutani & Smith, 1979; Tsurutani et al., 1996).

The averaged profiles reveal that the CSs are statistically asymmetric with a few percent difference in the magnetic field magnitude at the CS boundaries, mostly due to the asymmetry of the maximum variance component. About 9.4% of the CSs were classified as bifurcated: magnetic field rotation is relatively smooth across non-bifurcated CSs, while occurs in two steps across bifurcated CSs. Both types of CSs have almost identical statistical distributions of the CS asymmetry and relative variations of the magnetic field magnitude, but bifurcated CSs tend to have larger scales. The 5th and 95th percentiles of the CS half-thickness are about 200 and 2,000 km for non-bifurcated CSs, while the corresponding quantifies for bifurcated CSs are about 500 and 5,000 km (Figure 3). The current density in the CSs is typically 0.05–0.5 nA/m^2 and dominated by the component parallel to local magnetic field (Figures 4 and 6). The average perpendicular current density is typically less than 10% of the total current density, but along with magnetic field magnitude variations tends to be larger for CSs observed at larger plasma beta (Figure 4).

The CSs are predominantly proton kinetic-scale structures with spatial scales of the order of local proton inertial length. The 5th and 95th percentiles of the CS half-thickness are about 0.5 and $5\lambda_p$ for non-bifurcated CSs and about 0.7 and $15\lambda_p$ for bifurcated CSs. Note that the CSs have similar scales in units of thermal proton gyroradius $\rho_p = \lambda_p\beta_p^{1/2}$, because proton beta β_p was around one (Figure 5). The parallel current density amplitude in the CSs is strongly correlated with local Alfvén current density $J_A = en_eV_A$ and typically resides between about 0.04 and $0.4J_A$ with the median value of about $0.1J_A$. The electron-ion drift velocity corresponding to the observed current density amplitudes is then typically between 0.04 and 0.4 of local Alfvén speed V_A or local ion-acoustic speed $c_{\rm IA}$, because electron beta β_e is around one (Figure 1) and we have $c_{\rm IA} = V_A(\beta_e/2)^{1/2} \approx V_A$. Since electron to ion temperature ratio is also around one (Figure 1), the estimated electron-ion drift velocities are well below the threshold of the ion-acoustic instability (e.g., Boldyrev et al. (2015)). We expect therefore the CSs observed at 5 AU to be stable to the ion-acoustic instability.

The CSs exhibit a sort of scale-invariance in that several properties are correlated with the half-thickness in approximately a power law fashion (Figure 7 and Eq. (4)). We discuss only the scale-invariance of the shear angle $\Delta\theta \approx 16.6^\circ(\lambda/\lambda_p)^{0.34}$, since the observed scale-invariance of normalized magnetic field and current density amplitudes can be deduced by noticing that $\Delta B_x/\langle B\rangle \approx 2\sin(\Delta\theta/2) \approx \Delta\theta$ and $J_0/J_A \approx \Delta\theta(2\lambda/\lambda_p)^{-1}$. The scale-invariance of the shear angle is practically consistent with the scaling of the mean shear angle with the temporal half-thickness, $\langle\Delta\theta\rangle \approx 13.4^\circ\tau_{\rm CS}^{0.38} \approx 10.3^\circ(2\tau_{\rm CS})^{0.38}$ (Figure 8c) that is certainly not surprising, since according to the Taylor hypothesis we have $\lambda = V_n\tau_{\rm CS}$. Note that a positive correlation between $\Delta\theta$ and $\tau_{\rm CS}$ was previously pointed out, but not quantified, by Miao et al. (2011). The revealed scale-invariance indicates that the CSs are highly-likely produced by turbulence cascade (Boldyrev, 2005; Vasko et al., 2022). This hypothesis was further supported by matching the magnetic field rotation angle and compressibility in the CSs against equivalent properties of all the magnetic field fluctuations observed over the considered 641 days. The magnetic field rotation angles α_τ on different temporal scales τ were shown to be approximately self-similar, because the PDFs of α_τ practically collapsed to a universal distribution once at every scale τ we normalized angles α_τ to corresponding mean value $\langle\alpha_\tau\rangle$ (Figure 8a,b). Similar self-similarity was reported for magnetic field rotations (Zhdankin et al., 2012; Chen et al., 2015) and increments (Kiyani et al., 2009; Alberti et al., 2020; Chhiber et al., 2021) at 1 AU and near the Sun, and is considered a strong evidence for turbulence cascade development (e.g., Bruno and Carbone (2013)). The fact that the scaling of the mean rotation angle with temporal scale, $\langle\alpha_\tau\rangle \approx 1.3^\circ\tau^{0.35}$, is similar to the scaling revealed for the CSs strongly indicates that the CSs are produced by turbulence. We also demonstrated that magnetic field compressibility within the CSs is practically identical with that of ambient magnetic field fluctuations at comparable temporal scales (Figure 9). Note that the magnetic field compressibility tends to be larger for smaller scale CSs (Figure 9e) and at larger betas (Figure 4). The CSs are therefore following the trends well established for solar wind turbulence at 1 AU in that the compressibility increases toward smaller scales and at larger plasma betas (Smith et al., 2006; Hamilton et al., 2008; Podesta, 2009; Chen, 2016). We may speculate therefore that the compressibility observed *within* the CSs is inherited from ambient turbulence. In quite a contrast, the compressibility computed *between* the CS boundaries and quantified by $\chi_{\rm CS}^{\rm b} \approx 0.5(\Delta B/\langle B\rangle\Delta\theta)^2$ is statistically much lower than observed in ambient solar wind (Figure 9). In other words, the ratio between average perpendicular and parallel current densities $J_{\perp}/J_{||} \approx \Delta B/\langle B\rangle\Delta\theta$ is typically much smaller within the CSs than in ambient solar wind at comparable temporal scales.

The relatively low temporal resolution of plasma measurements aboard Ulysses did not allow us to estimate the fraction of reconnecting CSs in our dataset. Note that a bifurcated magnetic field profile does not necessarily imply magnetic reconnection and vice versa magnetic reconnection does not always imply a bifurcated profile (Gosling & Szabo, 2008; Phan et al., 2020). The previous observations at 1 AU and near the Sun showed that the occurrence of magnetic reconnection is about a few percent (Gosling, 2012; Osman et al., 2014; Eriksson et al., 2022; Fargette et al., 2023). If similar occurrence is typical at 5 AU, there should be a few hundred reconnecting CSs in our dataset. While the factors controlling magnetic reconnection in the solar wind are still not entirely established, here we considered whether magnetic reconnection can be suppressed through the diamagnetic drift of X-line resulting from different values of plasma beta at the CS boundaries (Swisdak et al., 2003; Swisdak et al., 2010). Note that this mechanism was previously shown to control magnetic reconnection at the Earth's magnetopause (Phan et al., 2013) and highly likely at the Saturn's magnetopause (Masters et al., 2012). We showed that the difference $\Delta\beta$ between plasma betas at the CS boundaries is typically too low to suppresses magnetic reconnection. Only 5–11% of the CSs have $\Delta\beta$ sufficiently high to suppress magnetic reconnection, while for most of the CSs magnetic reconnection is, in principle, allowed (Figure 10). This *does not* imply however that magnetic reconnection will always occur, since most likely it will be suppressed by other processes like the shear of plasma flow velocity (Doss et al., 2015; Phan et al., 2020) or relatively slow reconnection rate compared to turbulence nonlinear time (e.g., Zhdankin et al. (2013); Boldyrev and Loureiro (2020)).

We collected CSs using the PVI methodology (Greco et al., 2008, 2018), but used only the PVI index corresponding to the smallest time increment dictated by data resolution and applied the PVI threshold of 5. This methodology is identical to that used previously at 0.2 and 1 AU (Vasko et al., 2021, 2022; Lotekar et al., 2022). The use of PVI indexes corresponding to larger time increments would not substantially expand our dataset, because high PVI events of different temporal scales are typically nested into each other (Greco et al., 2016) and the 1 min window around points with PVI$>$ 5 in our selection procedure allows identifying coherent structures with up to ≈1 min scales. Our dataset could be expanded however by lowering the PVI threshold and identifying CSs with smaller current density and, hence, larger scales, since $J_0 \propto \lambda^{-0.66}$ (Figure 7). Even though our dataset is biased toward smaller scale CSs, we believe most of CSs present at 5 AU has been captured, because the revealed occurrence rate is consistent with previous reports at 5 AU, where different selection procedures were implemented (Tsurutani et al., 1996; Erdős & Balogh, 2008; Miao et al., 2011). Before conclusion we point out that our analysis was solely devoted to CSs, while other coherent structures, not least important for solar wind dynamics, such as flux ropes and Alfvén vortexes (Roberts et al., 2016; Perrone et al., 2017; Zhao et al., 2021) were excluded by requiring magnetic field profiles typical of CSs.

5 Conclusion

We presented a statistical analysis of 16,903 CSs observed over 641 days aboard Ulysses spacecraft at 5 AU, close to the ecliptic plane and around solar minimum. The results of this study can be summarized as follows.

1. The CSs are essentially magnetic field rotations, with relatively small variations of the magnetic field magnitude and predominantly parallel (magnetic field-aligned) current density. For more than 90% of the CSs we have $\Delta B/\langle B\rangle \lesssim 0.1$ for the relative magnetic field magnitude variation between the CS boundaries, $\Delta B_{\rm max}/\langle B\rangle \lesssim 0.2$ for the maximum relative variation within CS, and $\Delta B/\langle B\rangle\Delta\theta \lesssim 0.1$ for the ratio between average perpendicular and parallel current densities (Eq. (3)). The relative magnetic field magnitude variations and perpendicular current density tend to be larger at higher plasma beta.

2. The CSs are typically asymmetric with statistically different magnitudes of the maximum variance component B_x, which reverses sign across CS, at the CS boundaries. For more than 50% of the CSs we have $\langle B_x\rangle/\Delta B_x \gtrsim 0.1$, where $\langle B_x\rangle$ is the mean of B_x values at the CS boundaries, while ΔB_x is their difference.

3. About 9.4% of the CSs were classified as bifurcated. Both types of CSs have basically identical statistical distributions of the CS asymmetry and relative variations of the magnetic field magnitude.

4. The CSs are proton kinetic-scale structures. For non-bifurcated CSs the 5th and 95th percentiles of the half-thickness are respectively about 200 and 2,000 km or 0.5 and $5\lambda_p$ in units of local proton inertial length. Similar quantities for bifurcated CSs are about 500 and 5,000 km or 0.7 and $15\lambda_p$.

5. The current density observed in the CSs is strongly correlated with local Alfvén current density. The 5th and 95th percentiles of the current density amplitude are about 0.05 and 0.5 nA/m^2 or 0.04 and $0.4J_A$ in units of local Alfvén current density. The electron-ion drift velocity within the CSs is well below the ion-acoustic instability threshold.

6. The CSs exhibit a sort of scale-invariance (Figures 7 and 8). The shear angle scales with spatial and temporal half-thickness: $\Delta\theta \approx 16.6^\circ(\lambda/\lambda_p)^{0.34}$ and $\langle\Delta\theta\rangle \approx 13.4^\circ\tau_{\rm CS}^{0.38} \approx 10.3^\circ(2\tau_{\rm CS})^{0.38}$, where in our dataset $\tau_{\rm CS}$ is predominantly between 1 and 60s.

7. The magnetic field rotation and compressibility within the CSs are quite similar to those typical of ambient magnetic field fluctuations (Figures 8 and 9). The scaling $\langle\alpha_\tau\rangle \approx 1.3^\circ\tau^{0.35}$ of the mean rotation angle $\langle\alpha_\tau\rangle$ at temporal scale τ observed for all magnetic field rotations in the solar wind is quite similar to the scaling $\langle\Delta\theta\rangle \approx 10.3^\circ(2\tau_{\rm CS})^{0.38}$ revealed for the CSs.

8. For most of the CSs the asymmetry of plasma beta between the CS boundaries is insufficient to suppress magnetic reconnection through the diamagnetic drift of X-line. Even though typically allowed by this condition, magnetic reconnection can be suppressed or controlled by other mechanisms not considered in this study.

In conclusion, the CSs observed at 5 AU are typically magnetic field rotations on proton kinetic scales. There are strong indications that these structures are produced by turbulence, inheriting scale-invariance and compressibility. The observed asymmetry in plasma beta is insufficient to suppress magnetic reconnection in the CSs, but other processes not considered here may suppress or control it. The presented results will be of value of future comparative analyses of current sheets observed at different radial distances from the Sun.

Data Availability Statement

The list of all current sheets considered in this paper is available at Vasko et al. (2024). The Ulysses data used in this paper are publically available at https://www.cosmos.esa.int/web/ulysses.

Acknowledgments

The work of T.P. was supported by NASA Living With a Star grant No. 80NSSC20K1781. The work of F.M. was supported by NASA Heliophysics Guest Investigator grant No. 80NSSC21K0730. The work of A.A. was supported by NASA Living With a Star grant No. 80NSSC20K1788. I.V. thanks Russian Science Foundation grant No. 21-12-00416.

References

Alberti, T., Laurenza, M., Consolini, G., Milillo, A., Marcucci, M. F., Carbone, V., & Bale, S. D. (2020, October). On the Scaling Properties of Magnetic-field Fluctuations through the Inner Heliosphere. *Astrophys. J.*, *902*(1), 84. doi: 10.3847/1538-4357/abb3d2

Artemyev, A. V., Angelopoulos, V., Halekas, J. S., Vinogradov, A. A., Vasko, I. Y., & Zelenyi, L. M. (2018, Jun). Dynamics of Intense Currents in the Solar Wind. *Astrophys. J.*, *859*(2), 95. doi: 10.3847/1538-4357/aabe89

Artemyev, A. V., Angelopoulos, V., & Vasko, I. Y. (2019, June). Kinetic Properties of Solar Wind Discontinuities at 1 AU Observed by ARTEMIS. *Journal of Geophysical Research (Space Physics)*, *124*(6), 3858-3870. doi: 10.1029/2019JA026597

Artemyev, A. V., Angelopoulos, V., Vasko, I. Y., Runov, A., Avanov, L. A., Giles, B. L., ... Strangeway, R. J. (2019, February). On the Kinetic Nature of Solar Wind Discontinuities. *Geophys. Res. Lett.*, *46*(3), 1185-1194. doi: 10.1029/2018GL079906

Balogh, A., Beek, T. J., Forsyth, R. J., Hedgecock, P. C., Marquedant, R. J., Smith, E. J., ... Tsurutani, B. T. (1992, January). The magnetic field investigation on the ULYSSES mission - Instrumentation and preliminary scientific results. *Astronomy and Astrophysics Suppl. Series*, *92*(2), 221-236.

Bame, S. J., McComas, D. J., Barraclough, B. L., Phillips, J. L., Sofaly, K. J., Chavez, J. C., ... Sakurai, R. K. (1992, January). The ULYSSES solar wind plasma experiment. *Astronomy and Astrophysics Suppl. Series*, *92*(2), 237-265.

Bieber, J. W., Wanner, W., & Matthaeus, W. H. (1996, February). Dominant two-dimensional solar wind turbulence with implications for cosmic ray transport. *J. Geophys. Res.*, *101*(A2), 2511-2522. doi: 10.1029/95JA02588

Boldyrev, S. (2005, June). On the Spectrum of Magnetohydrodynamic Turbulence. *Astrophys. J. Lett.*, *626*(1), L37-L40. doi: 10.1086/431649

Boldyrev, S., Chen, C. H. K., Xia, Q., & Zhdankin, V. (2015, June). Spectral Breaks of Alfv&eacutenic Turbulence in a Collisionless Plasma. *Astrophys. J.*, *806*(2), 238. doi: 10.1088/0004-637X/806/2/238

Boldyrev, S., & Loureiro, N. F. (2020, September). Tearing Instability in Alfvén and Kinetic-Alfvén Turbulence. *Journal of Geophysical Research (Space Physics)*, *125*(9), e28185. doi: 10.1029/2020JA028185

Borovsky, J. E. (2008, August). Flux tube texture of the solar wind: Strands of the magnetic carpet at 1 AU? *Journal of Geophysical Research (Space Physics)*, *113*(A8), A08110. doi: 10.1029/2007JA012684

Borovsky, J. E., & Burkholder, B. L. (2020, February). On the Fourier Contribution of Strong Current Sheets to the High-Frequency Magnetic Power SpectralDensity of the Solar Wind. *Journal of Geophysical Research (Space Physics)*, *125*(2), e27307. doi: 10.1029/2019JA027307

Borovsky, J. E., & Podesta, J. J. (2015, November). Exploring the effect of current sheet thickness on the high-frequency Fourier spectrum breakpoint of the solar wind. *Journal of Geophysical Research (Space Physics)*, *120*(11), 9256-9268. doi: 10.1002/2015JA021622

Bruno, R., & Carbone, V. (2013, May). The Solar Wind as a Turbulence Laboratory. *Living Reviews in Solar Physics*, *10*(1), 2. doi: 10.12942/lrsp-2013-2

Burlaga, L. F. (1969, April). Directional Discontinuities in the Interplanetary Magnetic Field. *Solar Physics*, *7*(1), 54-71. doi: 10.1007/BF00148406

Burlaga, L. F., Lemaire, J. F., & Turner, J. M. (1977, August). Interplanetary current sheets at 1 AU. *J. Geophys. Res.*, *82*, 3191-3200. doi: 10.1029/JA082i022p03191

Burlaga, L. F., & Ness, N. F. (1969, October). Tangential Discontinuities in the Solar Wind. *Solar Physics*, *9*(2), 467-477. doi: 10.1007/BF02391672

Chen, C. H. K. (2016, December). Recent progress in astrophysical plasma turbulence from solar wind observations. *Journal of Plasma Physics*, *82*(6), 535820602. doi: 10.1017/S0022377816001124

Chen, C. H. K., Matteini, L., Burgess, D., & Horbury, T. S. (2015, October). Magnetic field rotations in the solar wind at kinetic scales. *Monthly Notices of Royal Astronomy Society*, *453*(1), L64-L68. doi: 10.1093/mnrasl/slv107

Chhiber, R., Matthaeus, W. H., Bowen, T. A., & Bale, S. D. (2021, April). Subproton-scale Intermittency in Near-Sun Solar Wind Turbulence Observed by the Parker Solar Probe. *Astrophys. J. Lett.*, *911*(1), L7. doi: 10.3847/2041-8213/abf04e

Cuesta, M. E., Parashar, T. N., Chhiber, R., & Matthaeus, W. H. (2022, March). Intermittency in the Expanding Solar Wind: Observations from Parker Solar Probe (0.16 au), Helios 1 (0.3-1 au), and Voyager 1 (1-10 au). *Astrophys. J. Suppl. Series*, *259*(1), 23. doi: 10.3847/1538-4365/ac45fa

Doss, C. E., Komar, C. M., Cassak, P. A., Wilder, F. D., Eriksson, S., & Drake, J. F. (2015, September). Asymmetric magnetic reconnection with a flow shear and applications to the magnetopause. *Journal of Geophysical Research (Space Physics)*, *120*(9), 7748-7763. doi: 10.1002/2015JA021489

Erdős, G., & Balogh, A. (2008, January). Density of discontinuities in the heliosphere. *Advances in Space Research*, *41*(2), 287-296. doi: 10.1016/j.asr.2007.04.036

Eriksson, S., Swisdak, M., Weygand, J. M., Mallet, A., Newman, D. L., Lapenta, G., ... Larsen, B. (2022, July). Characteristics of Multi-scale Current Sheets in the Solar Wind at 1 au Associated with Magnetic Reconnection and the Case for a Heliospheric Current Sheet Avalanche. *Astrophys. J.*, *933*(2), 181. doi: 10.3847/1538-4357/ac73f6

Fargette, N., Lavraud, B., Rouillard, A. P., Houdayer, P. S., Phan, T. D., Øieroset, M., ... Horbury, T. S. (2023, June). Clustering of magnetic reconnection exhausts in the solar wind: An automated detection study. *Astronomy and Astrophysics*, *674*, A98. doi: 10.1051/0004-6361/202346043

Franci, L., Cerri, S. S., Califano, F., Landi, S., Papini, E., Verdini, A., ... Hellinger, P. (2017, November). Magnetic Reconnection as a Driver for a Sub-ion-scale Cascade in Plasma Turbulence. *Astrophys. J. Lett.*, *850*(1), L16. doi: 10.3847/2041-8213/aa93fb

Gosling, J. T. (2012, November). Magnetic Reconnection in the Solar Wind. *Space Sci. Rev.*, *172*, 187-200. doi: 10.1007/s11214-011-9747-2

Gosling, J. T., & Szabo, A. (2008, October). Bifurcated current sheets produced by magnetic reconnection in the solar wind. *Journal of Geophysical Research (Space Physics)*, *113*(A10), A10103. doi: 10.1029/2008JA013473

Greco, A., Chuychai, P., Matthaeus, W. H., Servidio, S., & Dmitruk, P. (2008, October). Intermittent MHD structures and classical discontinuities. *Geophys. Res. Lett.*, *35*, L19111. doi: 10.1029/2008GL035454

Greco, A., Matthaeus, W. H., Perri, S., Osman, K. T., Servidio, S., Wan, M., & Dmitruk, P. (2018, Feb). Partial Variance of Increments Method in Solar Wind Observations and Plasma Simulations. *Space Sci. Rev.*, *214*(1), 1. doi: 10.1007/s11214-017-0435-8

Greco, A., Matthaeus, W. H., Servidio, S., Chuychai, P., & Dmitruk, P. (2009, February). Statistical Analysis of Discontinuities in Solar Wind ACE Data and Comparison with Intermittent MHD Turbulence. *Astrophys. J. Lett.*, *691*(2), L111-L114. doi: 10.1088/0004-637X/691/2/L111

Greco, A., Perri, S., Servidio, S., Yordanova, E., & Veltri, P. (2016, June). The Complex Structure of Magnetic Field Discontinuities in the Turbulent Solar Wind. *Astrophys. J. Lett.*, *823*(2), L39. doi: 10.3847/2041-8205/823/2/L39

Hamilton, K., Smith, C. W., Vasquez, B. J., & Leamon, R. J. (2008, January). Anisotropies and helicities in the solar wind inertial and dissipation ranges at 1 AU. *Journal of Geophysical Research (Space Physics)*, *113*(A1), A01106. doi: 10.1029/2007JA012559

Horbury, T. S., Burgess, D., Fränz, M., & Owen, C. J. (2001, January). Three spacecraft observations of solar wind discontinuities. *Geophys. Res. Lett.*, *28*(4), 677-680. doi: 10.1029/2000GL000121

Jain, N., Büchner, J., Comişel, H., & Motschmann, U. (2021, October). Free Energy Sources in Current Sheets Formed in Collisionless Plasma Turbulence. *Astrophys. J.*, *919*(2), 103. doi: 10.3847/1538-4357/ac106c

Kiyani, K. H., Chapman, S. C., Khotyaintsev, Y. V., Dunlop, M. W., & Sahraoui, F. (2009, August). Global Scale-Invariant Dissipation in Collisionless Plasma Turbulence. *Phys. Rev. Lett.*, *103*(7), 075006. doi: 10.1103/PhysRevLett.103.075006

Knetter, T., Neubauer, F. M., Horbury, T., & Balogh, A. (2004, June). Four-point discontinuity observations using Cluster magnetic field data: A statistical survey. *Journal of Geophysical Research (Space Physics)*, *109*, A06102. doi: 10.1029/2003JA010099

Leamon, R. J., Matthaeus, W. H., Smith, C. W., Zank, G. P., Mullan, D. J., & Oughton, S. (2000, July). MHD-driven Kinetic Dissipation in the Solar Wind and Corona. *Astrophys. J.*, *537*(2), 1054-1062. doi: 10.1086/309059

Leamon, R. J., Smith, C. W., Ness, N. F., Matthaeus, W. H., & Wong, H. K. (1998, March). Observational constraints on the dynamics of the interplanetary magnetic field dissipation range. *J. Geophys. Res.*, *103*, 4775. doi: 10.1029/97JA03394

Lepping, R. P., & Behannon, K. W. (1986, August). Magnetic field directional discontinuities - Characteristics between 0.46 and 1.0 AU. *J. Geophys. Res.*, *91*, 8725-8741. doi: 10.1029/JA091iA08p08725

Lotekar, A. B., Vasko, I. Y., Phan, T., Bale, S. D., Bowen, T. A., Halekas, J., ... Mozer, F. S. (2022, April). Kinetic-scale Current Sheets in Near-Sun Solar Wind: Properties, Scale-dependent Features and Reconnection Onset. *Astrophys. J.*, *929*(1), 58. doi: 10.3847/1538-4357/ac5bd9

Mariani, F., Bavassano, B., Villante, U., & Ness, N. F. (1973, January). Variations of the occurrence rate of discontinuities in the interplanetary magnetic field. *J. Geophys. Res.*, *78*(34), 8011. doi: 10.1029/JA078i034p08011

Masters, A., Eastwood, J. P., Swisdak, M., Thomsen, M. F., Russell, C. T., Sergis, N., ... Krimigis, S. M. (2012, April). The importance of plasma β conditions for magnetic reconnection at Saturn's magnetopause. *Geophys. Res. Lett.*, *39*(8), L08103. doi: 10.1029/2012GL051372

Matthaeus, W. H., Goldstein, M. L., & Roberts, D. A. (1990, December). Evidence for the presence of quasi-two-dimensional nearly incompressible fluctuations in the solar wind. *J. Geophys. Res.*, *95*, 20673-20683. doi: 10.1029/JA095iA12p20673

Matthaeus, W. H., Wan, M., Servidio, S., Greco, A., Osman, K. T., Oughton, S., & Dmitruk, P. (2015, April). Intermittency, nonlinear dynamics and dissipation in the solar wind and astrophysical plasmas. *Philosophical Transactions of the Royal Society of London Series A*, *373*(2041), 20140154-20140154. doi: 10.1098/rsta.2014.0154

Miao, B., Peng, B., & Li, G. (2011, February). Current sheets from Ulysses observation. *Annales Geophysicae*, *29*(2), 237-249. doi: 10.5194/angeo-29-237-2011

Mistry, R., Eastwood, J. P., Phan, T. D., & Hietala, H. (2017, June). Statistical properties of solar wind reconnection exhausts. *Journal of Geophysical Research (Space Physics)*, *122*(6), 5895-5909. doi: 10.1002/2017JA024032

Neugebauer, M. (2006, April). Comment on the abundances of rotational and tangential discontinuities in the solar wind. *Journal of Geophysical Research (Space Physics)*, *111*, A04103. doi: 10.1029/2005JA011497

Osman, K. T., Matthaeus, W. H., Gosling, J. T., Greco, A., Servidio, S., Hnat, B., ... Phan, T. D. (2014, May). Magnetic Reconnection and Intermittent Turbulence in the Solar

Wind. *Phys. Rev. Lett.*, *112*(21), 215002. doi: 10.1103/PhysRevLett.112.215002

Osman, K. T., Matthaeus, W. H., Wan, M., & Rappazzo, A. F. (2012, June). Intermittency and Local Heating in the Solar Wind. *Phys. Rev. Lett.*, *108*(26), 261102. doi: 10.1103/PhysRevLett.108.261102

Papini, E., Franci, L., Landi, S., Verdini, A., Matteini, L., & Hellinger, P. (2019, January). Can Hall Magnetohydrodynamics Explain Plasma Turbulence at Sub-ion Scales? *Astrophys. J.*, *870*(1), 52. doi: 10.3847/1538-4357/aaf003

Perri, S., Goldstein, M. L., Dorelli, J. C., & Sahraoui, F. (2012, November). Detection of Small-Scale Structures in the Dissipation Regime of Solar-Wind Turbulence. *Phys. Rev. Lett.*, *109*(19), 191101. doi: 10.1103/PhysRevLett.109.191101

Perrone, D., Alexandrova, O., Roberts, O. W., Lion, S., Lacombe, C., Walsh, A., ... Zouganelis, I. (2017, November). Coherent Structures at Ion Scales in Fast Solar Wind: Cluster Observations. *Astrophys. J.*, *849*(1), 49. doi: 10.3847/1538-4357/aa9022

Phan, T. D., Bale, S. D., Eastwood, J. P., Lavraud, B., Drake, J. F., Oieroset, M., ... Velli, M. (2020, February). Parker Solar Probe In Situ Observations of Magnetic Reconnection Exhausts during Encounter 1. *Astrophys. J. Suppl. Series*, *246*(2), 34. doi: 10.3847/1538-4365/ab55ee

Phan, T. D., Gosling, J. T., Paschmann, G., Pasma, C., Drake, J. F., Øieroset, M., ... Davis, M. S. (2010, August). The Dependence of Magnetic Reconnection on Plasma β and Magnetic Shear: Evidence from Solar Wind Observations. *Astrophys. J. Lett.*, *719*, L199-L203. doi: 10.1088/2041-8205/719/2/L199

Phan, T. D., Paschmann, G., Gosling, J. T., Oieroset, M., Fujimoto, M., Drake, J. F., & Angelopoulos, V. (2013, January). The dependence of magnetic reconnection on plasma β and magnetic shear: Evidence from magnetopause observations. *Geophys. Res. Lett.*, *40*(1), 11-16. doi: 10.1029/2012GL054528

Podesta, J. J. (2009, June). Dependence of Solar-Wind Power Spectra on the Direction of the Local Mean Magnetic Field. *Astrophys. J.*, *698*(2), 986-999. doi: 10.1088/0004-637X/698/2/986

Podesta, J. J. (2017, March). The most intense current sheets in the high-speed solar wind near 1 AU. *Journal of Geophysical Research (Space Physics)*, *122*(3), 2795-2823. doi: 10.1002/2016JA023629

Qudsi, R. A., Maruca, B. A., Matthaeus, W. H., Parashar, T. N., Bandyopadhyay, R., Chhiber, R., ... Raouafi, N. (2020, February). Observations of Heating along Intermittent Structures in the Inner Heliosphere from PSP Data. *Astrophys. J. Suppl. Series*, *246*(2), 46. doi: 10.3847/1538-4365/ab5c19

Roberts, O. W., Li, X., Alexandrova, O., & Li, B. (2016, May). Observation of an MHD Alfvén vortex in the slow solar wind. *Journal of Geophysical Research (Space Physics)*, *121*(5), 3870-3881. doi: 10.1002/2015JA022248

Sioulas, N., Shi, C., Huang, Z., & Velli, M. (2022, August). Preferential Heating of Protons over Electrons from Coherent Structures during the First Perihelion of the Parker Solar Probe. *Astrophys. J. Lett.*, *935*(2), L29. doi: 10.3847/2041-8213/ac85de

Smith, C. W., Matthaeus, W. H., Zank, G. P., Ness, N. F., Oughton, S., & Richardson, J. D. (2001). Heating of the low-latitude solar wind by dissipation of turbulent magnetic fluctuations. *Journal of Geophysical Research: Space Physics*, *106*(A5), 8253-8272. Retrieved from `https://agupubs.onlinelibrary.wiley.com/doi/abs/10.1029/2000JA000366` doi: https://doi.org/10.1029/2000JA000366

Smith, C. W., Vasquez, B. J., & Hamilton, K. (2006, September). Interplanetary magnetic fluctuation anisotropy in the inertial range. *Journal of Geophysical Research (Space Physics)*, *111*(A9), A09111. doi: 10.1029/2006JA011651

Söding, A., Neubauer, F. M., Tsurutani, B. T., Ness, N. F., & Lepping, R. P. (2001, July). Radial and latitudinal dependencies of discontinuities in the solar wind between 0.3 and 19 AU and -80 deg and +10 deg. *Annales Geophysicae*, *19*(7), 681-686. doi: 10.5194/angeo-19-681-2001

Sonnerup, B. U. Ö., & Scheible, M. (1998). Minimum and Maximum Variance Analysis. *ISSI Scientific Reports Series*, *1*, 185-220.

Swisdak, M., Opher, M., Drake, J. F., & Bibi, F. A. (2010, feb). THE VECTOR DIRECTION OF THE INTERSTELLAR MAGNETIC FIELD OUTSIDE THE HELIOSPHERE. *The Astrophysical Journal*, *710*(2), 1769–1775. Retrieved from `https://doi.org/10.1088/0004-637x/710/2/1769` doi: 10.1088/0004-637x/710/2/1769

Swisdak, M., Rogers, B. N., Drake, J. F., & Shay, M. A. (2003, May). Diamagnetic suppression of component magnetic reconnection at the magnetopause. *Journal of Geophysical Research (Space Physics)*, *108*(A5), 1218. doi: 10.1029/2002JA009726

Tsurutani, B. T., Ho, C. M., Arballo, J. K., Smith, E. L., Goldstein, B. E., Neugebauer, M., ... Feldman, W. C. (1996, May). Interplanetary discontinuities and Alfvén waves at high heliographic latitudes: Ulysses. *J. Geophys. Res.*, *101*(A5), 11027-11038. doi: 10.1029/95JA03479

Tsurutani, B. T., & Smith, E. J. (1979, June). Interplanetary discontinuities - Temporal variations and the radial gradient from 1 to 8.5 AU. *J. Geophys. Res.*, *84*, 2773-2787. doi: 10.1029/JA084iA06p02773

Vasko, I. Y., Alimov, K., Phan, T., Bale, S. D., Mozer, F. S., & Artemyev, A. V. (2022, February). Kinetic-scale Current Sheets in the Solar Wind at 1 au: Scale-dependent Properties and Critical Current Density. *Astrophys. J. Lett.*, *926*(2), L19. doi: 10.3847/2041-8213/ac4fc4

Vasko, I. Y., Alimov, K., Phan, T. D., Bale, S. D., Mozer, F. S., & Artemyev, A. V. (2021, December). Kinetic-scale Current Sheets in the Solar Wind at 1 au: Properties and the Necessary Condition for Reconnection. *Astrophys. J. Lett.*, *923*(1), L19. doi: 10.3847/2041-8213/ac3f30

Vasko, I.. Y., Alimov, K., Phan, T. D., & Mozer, F. S., Artemyev, A. V (2024, February 26). Dataset of current sheets for "Kinetic-scale current sheets in the solar wind at 5 AU" [Dataset]. *Zenodo*. https://doi.org/10.5281/zenodo.10705178

Vasquez, B. J., Abramenko, V. I., Haggerty, D. K., & Smith, C. W. (2007, November). Numerous small magnetic field discontinuities of Bartels rotation 2286 and the potential role of Alfvénic turbulence. *Journal of Geophysical Research (Space Physics)*, *112*(A11), A11102. doi: 10.1029/2007JA012504

Wang, R., Vasko, I. Y., Phan, T., & Mozer, F. (2023, December). Solar wind current sheets: MVA inaccuracy and recommended single-spacecraft methodology. *arXiv e-prints*, arXiv:2312.06043. doi: 10.48550/arXiv.2312.06043

Wang, R., Vasko, I. Y., Phan, T. D., & Mozer, F. S. (2024). Solar wind current sheets: Mva inaccuracy and recommended single-spacecraft methodology. *Journal of Geophysical Research: Space Physics*, *129*(2), e2023JA032215. Retrieved from `https://agupubs.onlinelibrary.wiley.com/doi/abs/10.1029/2023JA032215` (e2023JA032215 2023JA032215) doi: https://doi.org/10.1029/2023JA032215

Wu, P., Perri, S., Osman, K., Wan, M., Matthaeus, W. H., Shay, M. A., ... Chapman, S. (2013, February). Intermittent Heating in Solar Wind and Kinetic Simulations. *Astrophys. J. Lett.*, *763*(2), L30. doi: 10.1088/2041-8205/763/2/L30

Zhao, L. L., Zank, G. P., Hu, Q., Telloni, D., Chen, Y., Adhikari, L., ... Raouafi, N. E. (2021, June). Detection of small magnetic flux ropes from the third and fourth Parker Solar Probe encounters. *Astronomy and Astrophysics*, *650*, A12. doi: 10.1051/0004-6361/202039298

Zhdankin, V., Boldyrev, S., & Mason, J. (2012, December). Distribution of Magnetic Discontinuities in the Solar Wind and in Magnetohydrodynamic Turbulence. *Astrophys. J. Lett.*, *760*, L22. doi: 10.1088/2041-8205/760/2/L22

Zhdankin, V., Uzdensky, D. A., Perez, J. C., & Boldyrev, S. (2013, July). Statistical Analysis of Current Sheets in Three-dimensional Magnetohydrodynamic Turbulence. *Astrophys. J.*, *771*(2), 124. doi: 10.1088/0004-637X/771/2/124

-